ACS OMEGA

Open Access

http://pubs.acs.org/journal/acsodf

Article

Provenance and Tectonic Setting of the Lower Cretaceous Huanhe Formation in the Northwestern Ordos Basin and Its Implications for Uranium Mineralization

Da Sun,* Huaming Li,* Fei Xia,* Fengjun Nie, Guangwen Huang, Zhibo Zhang, Fanmin Meng, Jiayong Pan, and Yujie Hu

Cite This: *ACS Omega* 2024, 9, 3324−3341

Read Online

ACCESS | Metrics & More | Article Recommendations

ABSTRACT: The Ordos Basin is an important sandstone-type uranium enrichment region in China, and the Lower Cretaceous Huanhe Formation has attracted significant attention as a newly discovered ore-bearing stratum. To elucidate the provenance, tectonic background, and sedimentary environment constraints on uranium enrichment in the Huanhe Formation sandstone-type uranium deposits, 10 representative sandstone samples from the study area were analyzed by using electron microscopy, X-ray fluorescence (XRF), inductively coupled plasma mass spectrometry (ICP-MS), and electron probe microanalysis. Independent uranium minerals in the Yihewusu area of Hangjin Banner were shown for the first time to be composed mainly of coffinite and titanium-uranium oxide, with trace amounts of pitchblende. The major element diagrams of the sandstone and ratios of Sr/Ba, V/Cr, and U/Th and enrichment factors of Mo and U revealed that the source rocks of the Huanhe Formation sandstone in the study area were intermediate-felsic igneous rocks. The tectonic setting is characterized as an active continental margin, with later deposition in brackish-to-marine water environments. The ore-bearing strata indicate a reducing environment, whereas the nonore-bearing strata indicate a weakly oxidizing environment. With reference to previous studies, the sedimentary material primarily originated from the medium-acidic intrusive rocks exposed in the northern portion of the basin, including the Daqing-Wula Mountains, the Yin Mountains, and middle-acidic intrusions along the eastern margin of the Alxa region in the western part of the basin. The uranium-rich granitic pluton of the source area contributed to the preenrichment of uranium in the target sandstone layer. Under oxidizing aqueous conditions, U^{6+} migration was activated, whereas under reducing aqueous conditions, U^{6+} was reduced to U^{4+}, resulting in eventual sedimentation of coffinite as ore.

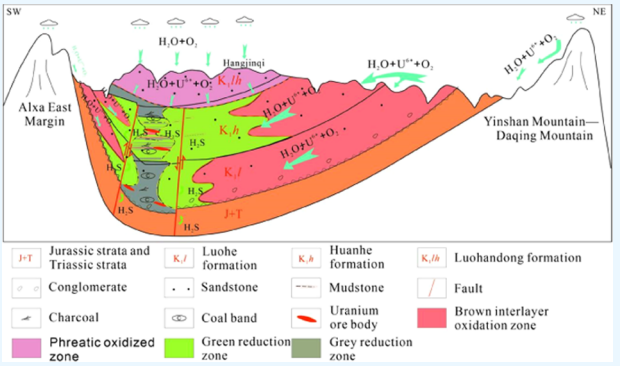

1. INTRODUCTION

The Ordos Basin is a significant multienergy resource basin in northern China and it hosts coal, uranium, oil, and natural gas deposits. Its formation is closely linked to the tectonic activities of three major structural domains: Paleo-Asia, Tethys, and Circum-Pacific.[1−3] The western segment of the northern part of the basin lies between the Yimeng Uplift and Tianhuan syncline structural units, which have undergone multiple phases of intense tectonic movement. These movements have posed challenges in determining the provenance of deposits and simultaneously introduced significant uncertainties in reservoir predictions for sandstone-type uranium deposits within the basin.[3−8] Detrital sediments are crucial indicators for deciphering the tectonic background of sedimentary basins, evolution of intracontinental basins, and characterization of source rock properties.[9−17] Sandstone-type uranium deposits exhibit distinct characteristics because the sand body is controlled by the facies and the ore is controlled by the sand body.[18] As a result, provenance investigations of sand bodies have become an essential prerequisite for conducting prospecting efforts targeting sandstone-type uranium deposits.

Lower Cretaceous strata have been extensively exposed in the northwestern part of the Ordos Basin. In recent years, with continued exploration for sandstone-type uranium deposits in northern regions, significant industrial uranium mineralization with relatively high grades (up to 16.44 kg/m^2) has been discovered within the Huanhe Formation sandstones in the

Received: August 22, 2023
Revised: December 18, 2023
Accepted: December 21, 2023
Published: January 10, 2024

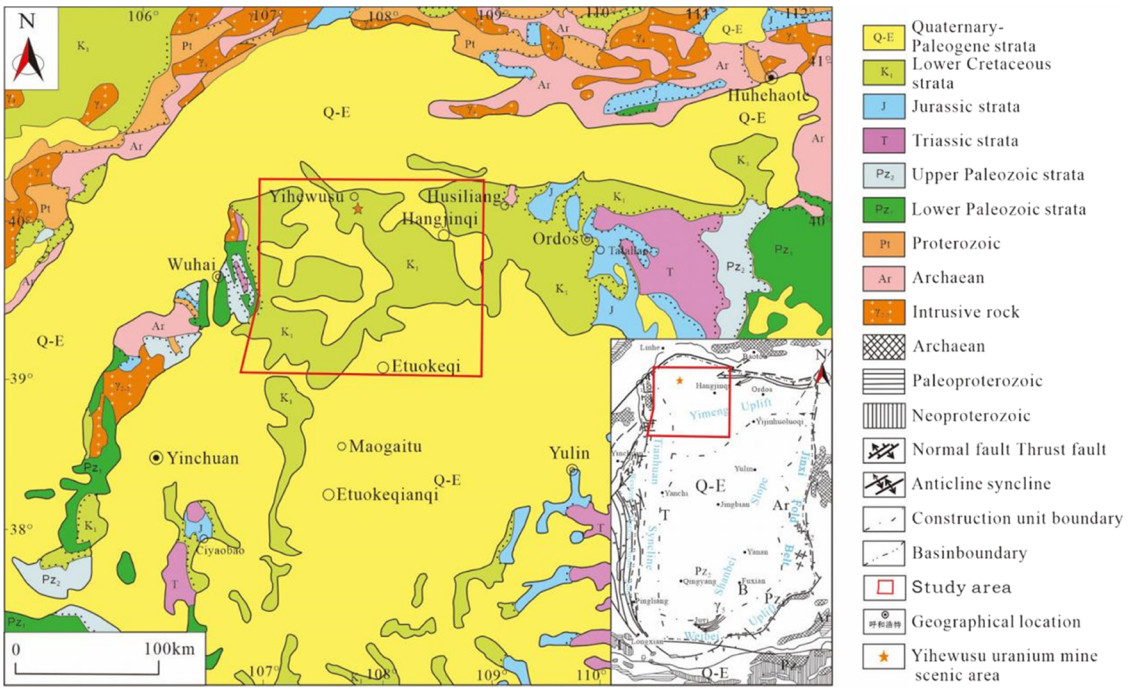

Figure 1. Geological map of the Northwestern Ordos Basin. (Revised by Wang et al.[19]) Adapted with permission from ref 19. Copyright: [Bulletin of Geological Science and Technology, 2023].

Yihewusu area of the northwestern Ordos Basin.[19] Subsequently, multiple industrial uranium-mineralized boreholes were identified, which further enhanced and solidified the exploration potential and scale of uranium mineralization in the Yihewusu area. Thus, the Huanhe Formation has been designated as a new prospecting horizon for mineral exploration in the Ordos Basin. Recently, scholars have focused on aspects such as the sedimentology and tectonic evolution of the Lower Cretaceous Huanhe Formation within the region.[19−27] However, research concerning detrital provenance and uranium mineralization characteristics within the area remains relatively limited, especially with regard to the occurrence characteristics of uranium minerals. Due to the limited research on the provenance and uranium mineralization, there has been a certain degree of constraint on the thorough exploration of sandstone-type uranium deposits within the region. Therefore, based on geological field surveys, this study systematically collected samples of the Huanhe Formation (mineralized) sandstone within the ore-bearing target layer in the Yihewusu area. Various methods were used to investigate these samples including petrology, elemental geochemistry, and electron probe microanalysis. By integrating previous research findings, this study preliminarily examined the provenance characteristics and uranium mineralization processes to provide an essential theoretical foundation for future sandstone-type uranium exploration efforts within this region.

2. GEOLOGICAL BACKGROUND

The Ordos Basin is a large-scale inland rift basin developed during the Mesozoic, and it covers an area of approximately 250,000 km^2, which is roughly equivalent to the sedimentary extent of the Late Mesozoic. The northern and southern margins of the basin are controlled by the Qilian−Qinling tectonic belt, which trends approximately east−west, and deep-seated fault zones along the margin of the Yinshan Mountains tectonic belt. The Taihang-Lvliang and Helan Mountains in the north−south tectonic belt constitute the eastern and western boundaries of the basin, respectively, and separate it from the Alxa and Shanxi Blocks. Thus, a rectangular basin with a north−south orientation was formed. The northern part of the basin is encircled by the Huanghe (Yellow River) fault depression and spans five provinces (Shaanxi, Gansu, Ningxia, Inner Mongolia, and Shanxi) and different regions.[25] During the Early Cretaceous, the Ordos Basin entered a state of stress relaxation following intense tectonic compression during the Yanshanian period. Early reverse fault inversion, accompanied by basic magmatic activity, marked the onset of a new evolutionary stage, thereby transforming the basin into a rift depression under extensional conditions. During this phase, the Ordos Basin largely inherited the paleogeographic pattern of the Late Jurassic half-graben depression with steep west and gentle east orientation. Within this context, the basin accumulated Luohe Formation (K1l) and Huanhe Formation (K1h), with the depositional center located along the Etuokeqi-Jingchuan line.

In the study area, the Cretaceous sequence from top to bottom consists of the Jingchuan Formation (K1j), Luohandong Formation (K1lh), Huanhe Formation (K1h), and Luohe Formation (K1l) (Figure 1). These formations are composed of red argillaceous siltstone, red sandstone, gray-green (reddish-brown) sandstone, and red conglomerates. The sedimentary facies mainly consist of delta deposits, braided river deposits, and aeolian sand dune deposits. The sandstone-type uranium deposits of the Huanhe Formation are primarily enriched in grayish-brown sandstones, which transition from brown and reddish-brown to greenish sandstones. Within the area, two significant faults influenced the Lower Cretaceous sequence, namely, the Sanyanjing and Wulanjilinmiao faults. Both are east−west-trending normal faults that cut through the Lower Cretaceous strata and underlying formations. These faults provide pathways for the migration of deep-seated

https://doi.org/10.1021/acsomega.3c06163
ACS Omega 2024, 9, 3324−3341

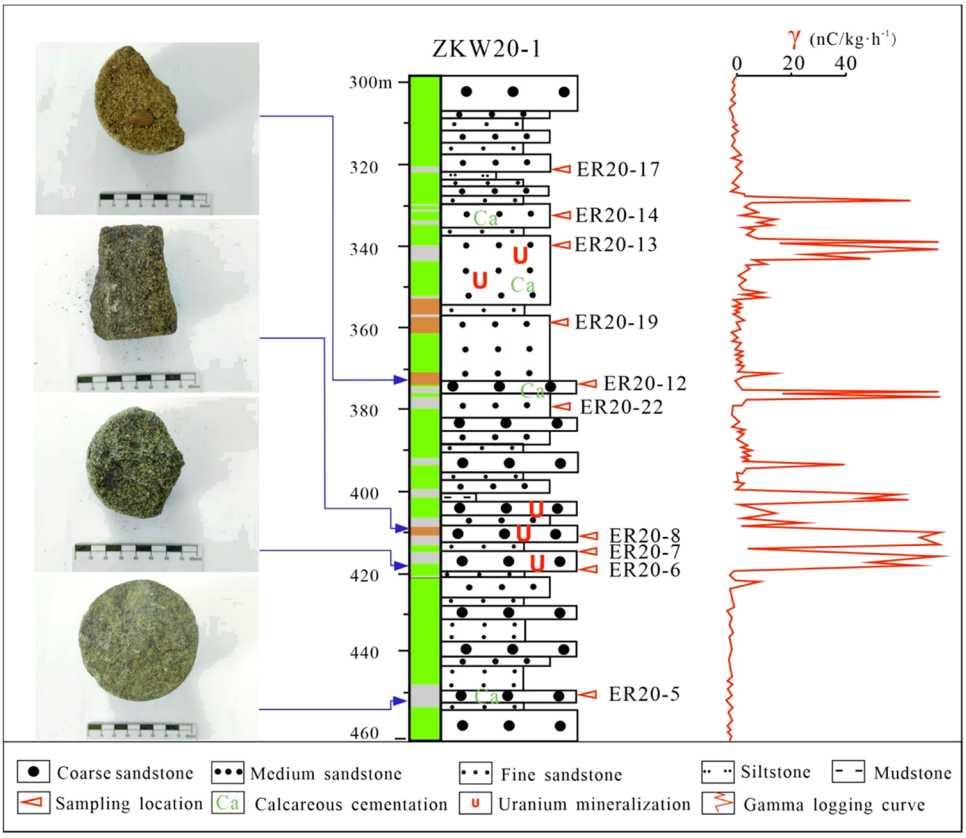

Figure 2. Borehole histogram of the Yihewusu region.

reducing gases and act as conduits for the discharge of oxygenated, uranium-bearing waters.[20,26,27]

3. MATERIALS AND METHODS

3.1. Materials and Preprocessing. Ten sandstone samples were selected from borehole ZKW20-1 from the Huanhe Formation in the Yihewusu area of the northwestern Ordos Basin. Among them, four samples were uranium-bearing sandstone, and six samples were regular sandstone (Figure 2). Sample preparation involving thin section and probe section preparation for the 10 samples was conducted at the sample preparation facility of the East China University of Technology. Subsequently, eight samples were selected, rock blocks from the samples were broken and ground using an agate mortar to a fineness of 200 mesh, and approximately 30 and 50 g of each sample were weighed. The samples were securely packaged in sample bags and sent to the State Key Laboratory of Nuclear Resources and Environment at the East China University of Technology for analysis and testing.

3.2. Thin Section Identification and Electron Probe Analysis. Mineral identification work was performed on 10 regular thin sections and 10 electron probe microanalysis (EPMA) thin sections of the Huanhe Formation sandstones at the State Key Laboratory of Nuclear Resources and Environment, East China University of Technology, using an electron microscope (Zeiss Axio Imager M2m). The chemical composition of the uranium minerals at the microscale was analyzed in an electron probe analysis chamber by using a JXA-8100 M electron probe coupled with an Inca energy-type energy dispersive spectrometer (EDS). The test conditions included an acceleration voltage of 15.0 kV, a beam current of 20.0 nA, a beam diameter of 2 μm, and a ZAF correction mode. The testing process strictly adhered to national standards (GB/T 15617-2002).[28]

3.3. Major Element Analysis. Major elemental analysis of the Huanhe Formation sandstone was conducted using an X-ray fluorescence spectrometer (Philips PW2404). Prior to geochemical analysis, the samples were crushed into a powder that could filter through 200 mesh. Samples (1−1.5 g) were accurately weighed and then heated in a ceramic crucible for 4 h. After being cooled for 2 h, the samples (0.5 ± 0.05 g) were weighed and placed in plastic cups. $Li_2B_4O_7$ and the cosolvent were poured dropwise into the sample holder and heated for 15 min. The prepared samples were tested in a Rigaku 100e XRF instrument, which had an analytical precision greater than 10%.

3.4. Trace Element Analysis. Trace and rare-earth element analyses of the Huanhe Formation sandstone were conducted using inductively coupled plasma mass spectrometry (ICP-MS) with a Thermo Fisher X Series II quadrupole plasma mass spectrometer. The samples were pretreated by using the acid dissolution method. First, 200 mesh samples were dried at 105 °C for 3 h. Then, 50 ± 1 mg of samples were weighed in a poly(tetrafluoroethylene) dissolution container and dissolved dropwise by adding HNO_3, HF, and $HClO_4$. Finally, the Rh internal standard solution was added, and the final solution was diluted to 100.0 g with deionized water such that the concentration of Rh in the solution was 10 ng/mL. The analytical precision was greater than 5%.[29]

4. RESULTS

4.1. Petrographic Characteristics. The exposed sandstones of the Huanhe Formation (K1h) are mainly composed of green and gray-green sandstones (Figure 3a). They exhibit

https://doi.org/10.1021/acsomega.3c06163
ACS Omega 2024, 9, 3324−3341

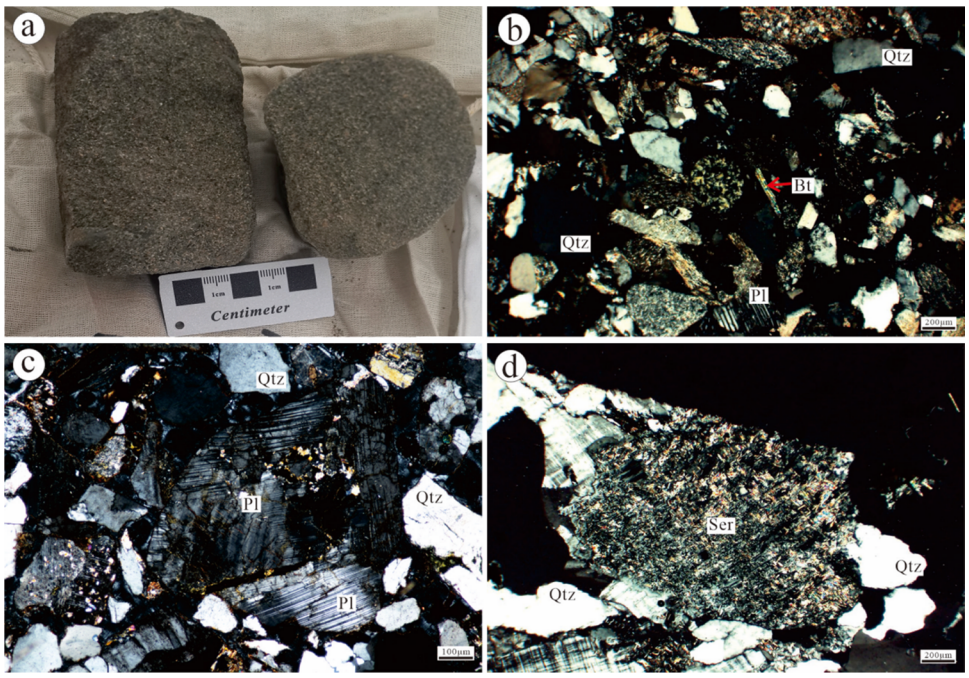

Figure 3. Rock photos and microscopic photos of sandstones from the Huanhe Formation in the Yihewusu area, Ordos Basin. (a) Green sandstone; (b) sand-like structure; (c) clear intracrystalline fracturing of feldspar; and (d) prominent sericitization of plagioclase; Qtz—quartz; Pl—plagioclase; Bt—biotite; Ser—sericite.

Table 1. Analysis Results of Major Elements in the Sandstone Samples from the Study Area[a]

sample no.	ER20-19	ER20-5	ER20-17	ER20-6	ER20-14	ER20-8	ER20-12	ER20-22	
lithology	brownish-red medium sandstone	gray calcareous fine sandstone	gray medium sandstone	green coarse sandstone	green medium sandstone	brownish-red coarse sandstone	brownish-red coarse sandstone	gray fine sandstone	upper crust
SiO_2	72.25	55.75	72.19	72.54	68.44	73.34	70.74	67.15	65.89
Al_2O_3	12.94	9.47	12.74	12.49	12.41	12.09	12.88	12.76	15.17
Fe_2O_3	1.77	1.45	0.86	0.87	1.61	0.77	0.57	1.87	
FeO	1.10	1.06	1.02	1.45	2.00	1.27	1.52	2.36	
MgO	1.23	1.28	0.79	1.20	1.75	0.76	0.67	2.51	2.20
CaO	1.73	13.38	2.34	1.77	2.98	2.05	2.46	1.96	4.19
Na_2O	3.40	2.72	3.46	3.76	3.69	3.69	4.18	3.41	3.89
K_2O	2.36	1.88	2.72	2.69	2.08	2.56	2.63	2.31	3.39
MnO	0.10	0.29	0.11	0.12	0.16	0.12	0.15	0.14	0.07
TiO_2	0.36	0.34	0.26	0.23	0.46	0.35	0.30	0.45	0.50
P_2O_5	0.09	0.08	0.09	0.09	0.11	0.10	0.11	0.11	0.20
loss on ignition	2.35	11.97	3.00	2.38	3.88	2.38	3.10	4.36	
CIA	53.87	46.27	50.12	50.80	47.89	49.46	48.01	52.78	49.21
CIW	60.29	51.40	56.72	57.65	52.46	55.82	53.71	58.88	
ICV	1.25	3.79	1.25	1.31	1.62	1.29	1.31	1.57	

[a]Notes: Chemical index of alteration (CIA) = $100 \times Al_2O_3/(Al_2O_3 + CaO^* + Na_2O + K_2O)$; chemical index of weathering (CIW) = $100 \times Al_2O_3/(Al_2O_3 + CaO^* + Na_2O)$; and index of compositional variability (ICV) = $(Fe_2O_3 + K_2O + Na_2O + CaO + MgO + MnO + TiO_2)/Al_2O_3$. Higher values indicate stronger weathering.[31,32] The chemical composition of the formula is the mole number, and CaO* refers to the CaO present in silicate minerals. When the mole number of CaO was greater than that of Na_2O, $mCaO^* = mNa_2O$. Otherwise, $mCaO^* = mCaO$.[33]

distinct sandstone structures (Figure 3b) and blocky fabrics. The clastic material is primarily composed of quartz, feldspar, and lithic fragments, with particle sizes ranging from 0.11 to 0.33 mm. The overall sortability is moderate to poor, and the roundness is relatively low. Quartz clasts are mostly single-crystal quartz that exhibit angular to subangular shapes, with a few displaying irregular shapes due to dissolution and significant intracrystalline fracturing (Figure 3c). They consist of 15−60% of clast content and show significant variations in the content. Feldspar clasts exhibit subangular shapes and account for 5−40% of the clast content, with extensive sericitization on their surfaces (Figure 3d). These optical characteristics indirectly suggest that the quartz and feldspar clasts were predominantly sourced from felsic igneous rocks. Debris accounts for 14−70% of the clast content and mainly includes granite and quartzite debris.

4.2. Major Element Characteristics. The elemental composition of sandstone from the Huanhe Formation in

https://doi.org/10.1021/acsomega.3c06163
ACS Omega 2024, 9, 3324−3341

Table 2. Trace Element Analysis Results for Sandstones from the Study Area (10^{-6})

sample no.	ER20-19	ER20-5	ER20-17	ER20-6	ER20-14	ER20-8	ER20-12	ER20-22	
lithology	brownish-red medium sandstone	gray calcareous fine sandstone	gray medium sandstone	green coarse sandstone	green medium sandstone	brownish-red coarse sandstone	brownish-red coarse sandstone	gray fine sandstone	upper crust
Li	15.80	13.80	18.10	15.60	22.00	17.30	15.80	42.70	20.00
Be	2.47	1.65	1.94	1.37	1.71	1.94	3.18	2.59	3.00
V	61.00	34.70	104.00	36.40	108.00	248.00	154.00	490.00	107.0
Cr	42.90	31.70	29.70	27.10	55.50	37.50	35.00	49.50	85.00
Co	6.40	6.13	20.10	11.10	9.01	16.10	27.70	11.00	17.00
Ni	15.40	12.60	18.90	14.90	19.10	22.40	35.50	25.90	44.00
Cu	8.27	7.58	564.00	8.58	8.86	8.15	21.80	15.40	25.00
Zn	31.70	27.60	28.20	32.20	45.50	432.00	39.70	299.00	71.00
Ga	14.00	10.70	14.50	13.30	14.00	12.80	13.20	17.40	17.00
Rb	64.50	47.10	73.30	69.20	59.20	67.70	70.00	73.30	112.0
Sr	332.00	335.00	333.00	337.00	396.00	312.00	344.00	472.00	350.0
Mo	0.70	0.45	0.52	0.57	1.28	116.00	3.07	38.00	1.50
Cd	0.05	0.04	0.04	0.23	0.09	2.44	0.19	2.01	0.10
In	0.03	0.03	0.04	0.03	0.06	0.03	0.02	0.05	0.05
Sb	0.41	0.36	1.04	0.38	0.52	1.77	1.03	1.45	0.20
Cs	2.82	1.65	3.27	2.55	3.68	2.64	3.40	5.22	4.60
Ba	698.00	619.00	727.00	824.00	579.00	769.00	1293.00	577.00	550.0
W	1.31	0.47	0.96	0.81	1.12	0.93	0.84	1.15	2.00
Tl	0.41	0.30	0.56	0.51	0.38	0.89	0.68	0.69	0.75
Pb	17.20	32.70	29.20	24.30	23.80	46.70	25.10	51.40	17.00
Bi	0.09	0.10	0.19	0.17	0.24	0.11	0.12	0.19	0.13
Th	5.09	6.48	4.17	5.70	6.87	6.14	5.19	7.55	10.70
U	3.47	2.64	48.30	11.80	38.10	700.00	679.00	954.00	2.80

Table 3. Rare-Earth Element Analysis Results for the Sandstone Samples from the Study Area (10^{-6})

sample no.	ER20-19	ER20-5	ER20-17	ER20-14	ER20-8	ER20-12	ER20-22		
lithology	brownish-red medium sandstone	gray calcareous fine sandstone	gray medium sandstone	green medium sandstone	brownish-red coarse sandstone	brownish-red coarse sandstone	gray fine sandstone	upper crust	lower crust
La	20.70	21.80	24.80	25.50	18.20	21.60	23.40	30.00	11.00
Ce	37.00	42.00	61.50	51.00	36.90	44.10	62.30	64.00	23.00
Pr	4.43	4.67	6.11	5.54	4.16	4.83	7.07	7.10	2.80
Nd	16.10	15.70	22.10	19.60	14.80	16.60	23.80	26.00	12.00
Sm	3.49	3.07	3.87	3.78	3.04	3.40	4.50	4.50	3.10
Eu	1.04	0.94	1.06	1.02	1.02	1.03	1.08	0.88	1.10
Gd	3.29	2.47	3.41	3.27	2.68	2.81	4.12	3.60	3.10
Tb	0.52	0.35	0.47	0.49	0.41	0.40	0.59	0.64	0.50
Dy	3.02	1.84	2.51	2.54	2.27	2.21	3.08	3.50	3.60
Ho	0.61	0.39	0.52	0.49	0.44	0.42	0.62	0.80	0.70
Er	1.79	1.23	1.57	1.51	1.27	1.28	1.83	2.30	2.20
Tm	0.30	0.18	0.24	0.23	0.19	0.21	0.29	0.33	0.30
Yb	1.72	1.15	1.45	1.39	1.14	1.30	1.67	2.20	2.20
Lu	0.26	0.18	0.21	0.21	0.17	0.20	0.25	0.32	0.20
∑REE	94.29	96.01	129.85	116.52	86.73	100.45	134.54	146.17	65.80
LREE	82.80	88.21	119.46	106.40	78.16	91.63	122.08	132.48	53.00
HREE	11.49	7.80	10.38	10.12	8.58	8.82	12.46	13.69	12.80
LREE/HREE	7.21	11.31	11.51	10.52	9.11	10.38	9.80	9.68	4.14
LaN/YbN	8.15	12.83	11.56	12.41	10.80	11.26	9.45		
LaN/SmN	3.74	4.45	4.03	4.25	3.77	4.01	3.27		
GdN/YbN	1.55	1.74	1.91	1.90	1.91	1.75	2.00		
δEu	0.93	1.01	0.88	0.87	1.07	0.99	0.75		
δCe	0.87	0.94	1.15	0.97	0.96	0.98	1.13		

the study area is presented in Table 1. In the sandstone in the Huanhe Formation, the SiO_2 content ranged from 55.75 to 73.34% (avg. of 69.5%), Al_2O_3 ranged from 9.47 to 12.94% (avg. of 12.22%), Fe_2O_3 ranged from 0.57 to 1.87% (avg. of 1.22%), FeO ranged from 1.02 to 2.36% (avg. of 1.47%), MgO ranged from 0.67 to 2.51% (avg. of 1.27%), Na_2O ranged from

https://doi.org/10.1021/acsomega.3c06163
ACS Omega 2024, 9, 3324−3341

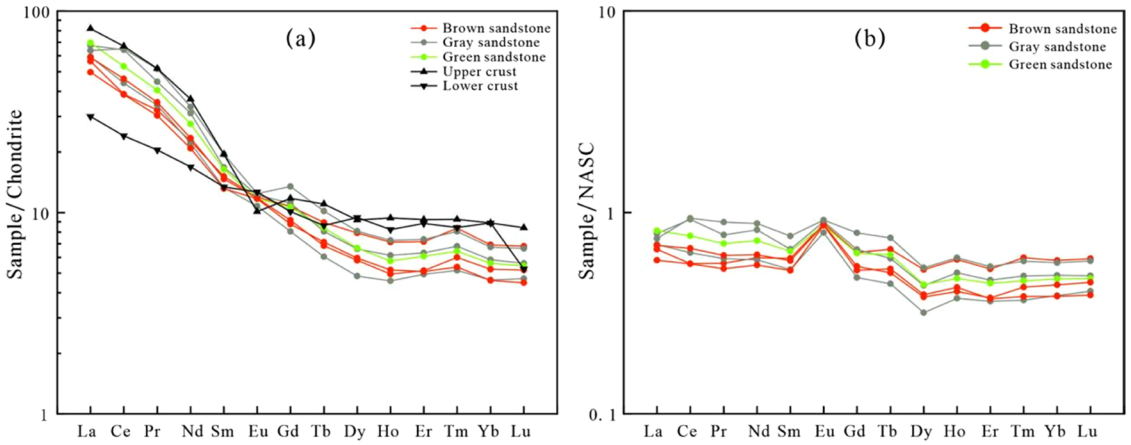

Figure 4. (a) Chondrite-normalized REE distribution pattern and (b) North American shale-normalized REE distribution pattern.

2.72 to 4.18% (avg. of 3.54%), K_2O ranged from 1.88 to 2.72% (avg. of 2.40%), MnO ranged from 0.10 to 0.29% (avg. of 0.15%), TiO_2 ranged from 0.23 to 0.46% (avg. of 0.34%), and P_2O_5 ranged from 0.08 to 0.11% (avg. of 0.10%). Substantial variations were observed in the CaO content, which ranged from 1.73 to 13.38% (average of 3.58%). Apart from the higher SiO_2 content compared with that of the continental upper crust, the remaining elements generally exhibited lower concentrations compared with those of the continental upper crust in the samples,[30] suggesting the presence of abundant quartz and clay constituents.

4.3. Trace and Rare-Earth Element Characteristics. The trace element data of the sandstone are given in Table 2. In terms of trace elements, the average Rb, Ba, and Sr contents were 65.54 × 10^{-6}, 760.10 × 10^{-6}, and 357.63 × 10^{-6}, respectively. Except for the slight enrichment of Ba compared with that in the continental upper crust, the remaining elements exhibited a weakly depleted pattern. The content of mafic elements, such as Cr and Ni, was slightly depleted compared to that in the upper crust, thus reflecting a higher proportion of acidic components in the sandstones in the study area.

The rare-earth element (REE) data for the sandstone samples are listed in Table 3. The total rare-earth elements (∑REE) in the sandstones of the Huanhe Formation in the Ordos Basin ranged from 86.73 to 134.54 × 10^{-6}, with an average value of 108.34 × 10^{-6}. The contents of light rare-earth elements (LREE) and heavy rare-earth elements (HREE) ranged from 78.16 to 122.08 × 10^{-6} and 7.80 to 12.46 × 10^{-6}, with average values of 98.39 × 10^{-6} and 9.95 × 10^{-6}, respectively. The LREE/HREE ratios varied between 7.21 and 11.51 × 10^{-6}, with an average value of 9.98 × 10^{-6}, indicating enrichment of LREEs and depletion of HREEs and notable fractionation between LREEs and HREEs. The chondrite-normalized REE distribution curve showed a significant rightward tilt and mild negative Eu anomalies (δEu = 0.75–1.07, with an average of 0.93; Figure 4a). The REE distribution curves of each sample were parallel to each other, indicating synchronous variations in the REE contents. The North American shale-normalized REE distribution curve displayed a nearly horizontal distribution feature (Figure 4b), indicating similarities in REE composition to North American shales. This suggests that the detrital source rocks within the study area originated from the continental upper crust.

4.4. Chemical Composition and Occurrence State of Uranium Minerals. The chemical composition and occurrence of uranium minerals in the ore-bearing sandstone of the research area were analyzed by using electron probe chemical composition analysis. The results are summarized in Table 4. The uranium minerals were mainly coffinite, followed by titanium-uranium oxide with a very small amount of pitchblende. The UO_2 content in coffinite ranged from 49.73 to 61.04%, with an average content of 53.74%; the SiO_2 content ranged from 16.30 to 21.12%, with an average content of 18.54%; the CaO content ranged from 0.90 to 2.89%, with an average content of 1.69%; the Y_2O_3 content ranged from 2.56 to 10.22%, with an average content of 5.96%; the P_2O_5 content ranged from 0.46 to 3.80%, with an average content of 2.35%; and the FeO content ranged from 0.14 to 4.90%, with an average content of 1.53%. Moreover, it also contained trace amounts of Na_2O, TiO_2, MgO, and Al_2O_3.

The UO_2 content in pitchblende ranged from 60.65 to 66.10%, with an average content of 63.37%; the SiO_2 content ranged from 8.45 to 11.98%, with an average content of 10.22%; the CaO content ranged from 2.34 to 3.21%, with an average content of 2.77%; the Y_2O_3 content ranged from 0.57 to 3.67%, with an average content of 2.12%; the P_2O_5 content ranged from 0.18 to 2.27%, with an average content of 1.22%; and the FeO content ranged from 0.25 to 0.73%, with an average content of 0.49%. In addition, trace amounts of Na_2O and Al_2O_3 were observed. The UO_2 content in titanium-uranium oxide ranged from 31.84 to 34.68%, with an average content of 33.20%; the TiO_2 content ranged from 24.11 to 41.38%, with an average content of 33.90%; and the SiO_2 content ranged from 7.41 to 14.39%, with an average content of 10.37%. Y_2O_3, P_2O_5, FeO, and SO_3 were found in some of the coffinite particles tested. This phenomenon could potentially be attributed to the relatively small size of the coffinite particles and their close association with xenotime and pyrite framboids, resulting in the inadvertent introduction of trace components during the testing procedure.

Electron probe backscattered electron (BSE) images of uranium minerals reveal that coffinite and pitchblende generally exhibit particle sizes ranging from 1 to 10 μm and display diverse morphologies and varied occurrences. Based on their morphological characteristics, distribution patterns, and associations with other minerals, these uranium minerals can be preliminarily classified based on five distinct occurrence patterns. (1) Uranium minerals were distributed along the

https://doi.org/10.1021/acsomega.3c06163
ACS Omega 2024, 9, 3324−3341

Table 4. Electron Probe Analysis Results of Uranium Minerals from Sandstone Samples from the Huanhe Formation in the Yihewusu area of the Ordos Basin[a]

test point	SiO_2	Al_2O_3	MgO	K_2O	CaO	TiO_2	ZrO_2	Y_2O_3	PbO	UO_2	Na_2O	P_2O_5	MnO	FeO	V_2O_3	total	type
20ER06-4	18.07	1.51	0.20	0.17	1.85	0.08	0.14	7.04	–	51.20	–	3.66	0.04	2.38	0.08	86.41	coffinite
20ER06-5	19.59	1.81	0.17	–	1.80	0.05	0.12	6.37	0.16	49.73	0.03	3.56	0.03	2.00	0.14	85.56	coffinite
20ER06-6	16.97	1.32	0.09	–	1.84	0.12	0.10	7.02	0.08	51.43	0.02	3.80	0.03	3.53	0.04	86.40	coffinite
20ER06-7	16.69	1.26	0.13	–	1.75	0.06	0.05	7.15	0.02	54.52	–	3.39	0.06	1.56	0.12	86.74	coffinite
20ER06-8	16.71	1.39	0.16	–	1.63	0.11	0.07	6.60	0.02	50.20	–	3.74	0.05	4.90	0.04	85.62	coffinite
20ER06-12	17.05	1.31	0.07	–	1.78	0.02	–	6.98	0.10	53.67	–	3.68	0.03	1.84	0.15	86.67	coffinite
20ER06-13	18.40	1.23	0.06	–	1.61	0.04	–	6.23	0.12	53.23	–	3.23	0.05	1.54	0.08	85.82	coffinite
20ER013-2	18.50	0.69	0.03	–	1.93	0.15	0.49	10.22	0.15	51.45	0.27	2.57	0.01	0.32	0.09	86.88	coffinite
20ER013-1	19.39	1.22	0.01	–	0.90	–	–	7.63	0.15	53.43	–	1.27	–	0.87	0.57	86.35	coffinite
20ER07-1	20.83	1.56	0.09	–	1.11	0.17	–	3.68	0.10	56.12	0.11	0.46	0.02	0.90	0.77	86.07	coffinite
20ER07-2	21.12	1.77	0.05	–	1.38	0.23	–	4.43	0.07	55.28	–	0.10	–	0.38	1.04	86.86	coffinite
20ER07-3	20.31	1.62	0.10	–	1.35	0.37	–	3.85	0.01	57.29	–	0.90	0.02	0.52	0.92	87.72	coffinite
20ER07-11	19.66	2.21	0.20	–	2.89	1.88	–	3.65	0.02	53.79	0.48	1.04	0.04	0.46	0.81	87.33	coffinite
20ER07-13	16.30	1.24	–	–	1.82	1.18	–	2.56	0.06	61.04	0.11	0.64	0.06	0.14	0.67	85.99	coffinite
20ER06-7	11.98	1.09	–	–	2.34	0.01	–	3.67	–	60.65	0.11	2.27	0.08	0.25	–	82.44	pitchblende
20ER06-10	8.45	0.20	–	–	3.21	1.57	0.50	0.57	0.05	66.10	0.08	0.18	0.30	0.73	0.04	81.97	pitchblende
20ER08-1	7.41	1.14	0.51	–	2.97	36.22	1.72	0.67	0.01	31.84	0.05	0.05	0.33	2.66	0.35	85.92	titanium-uranium oxide
20ER08-9	14.39	4.64	1.30	–	2.86	24.11	0.82	0.39	–	33.09	0.14	0.03	0.29	3.16	0.28	85.48	titanium-uranium oxide

[a]Notes. "–" represents below the detection limit.

https://doi.org/10.1021/acsomega.3c06163
ACS Omega 2024, 9, 3324−3341

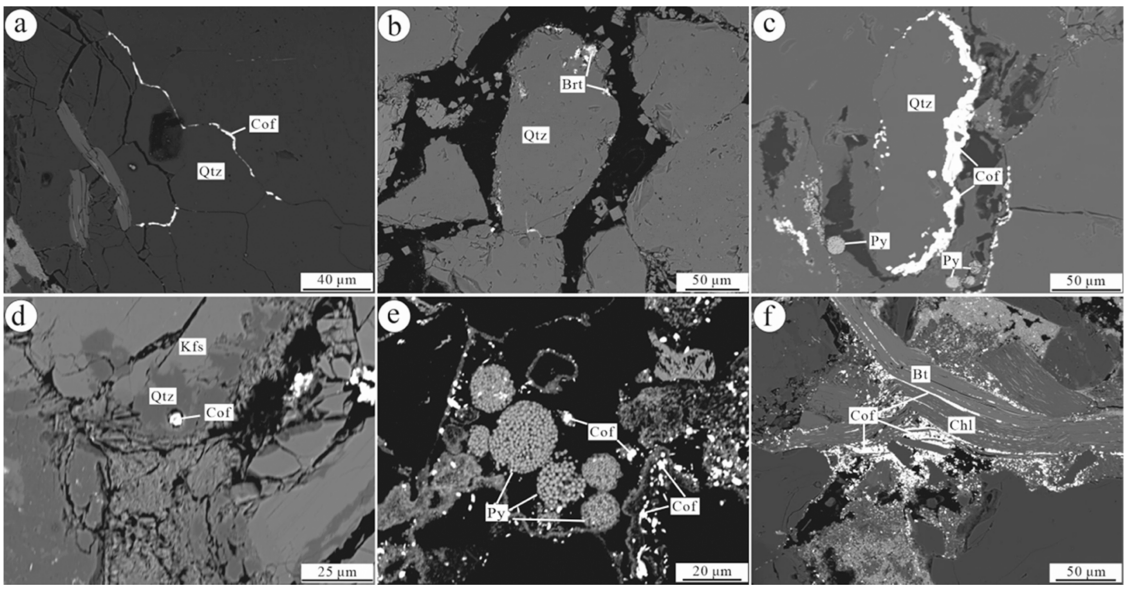

Figure 5. Backscatter images of uranium minerals from the sandstone of the Huanhe Formation in the Yihewusu area, Ordos Basin. (a) Coffinite distributed within quartz fractures; (b) titanium-uranium oxide distributed along quartz margins; (c) coffinite irregularly distributed at the periphery of quartz grains, creating an appearance of encirclement or inclusion; (d) coffinite distributed within quartz concavities; (e) coffinite distributed within fillings, coexisting with pyrite framboids; (f) coffinite coexisting with biotite and chlorite; Cof: coffinite; Qtz: quartz; Brt: titanium-uranium oxide; Py: pyrite; Kfs: potassium feldspar; Bt: biotite; Chl: chlorite.

edges of the detrital particles. This distribution pattern was predominantly observed at the edges and fractures of the quartz particles (Figure 5a,b). Coffinite occurred as irregular granular formations along the periphery of quartz particles, thus creating the illusion that the two formed a circle or package (Figure 5c). This portion of coffinite exhibited relatively larger grain sizes overall, accompanied by a higher content of UO_2. (2) Uranium minerals were distributed within detrital particles, with the main types of detrital particles being quartz, debris, and a minor amount of feldspar. Coffinite occurred as irregular granular formations or star-like clusters within the crystal lattice of detrital quartz. Coffinite was also found within the concavities of the quartz grains (Figure 5d). (3) Uranium minerals coexisted with pyrite framboids (Figure 5e) or limonite. Coffinite presented irregular, granular, and star-like patterns within the periphery of pyrite framboids and detrital quartz particles. The association of uranium minerals with pyrite and quartz was evident. When uranium minerals were distributed within quartz particles, the coexisting nearby pyrite could induce the reduction of precipitation owing to the strong reducing nature of pyrite, resulting in the reduction of the precipitation of U and SiO_2 from the fluid. (4) Uranium minerals were present around or within the cleavage fractures of biotite and coexisted with pyrite. This suggests that the Fe^{2+} contained in the biotite was capable of creating a favorable reducing microenvironment for the reduction and precipitation of U^{6+} (Figure 5f). (5) A small amount of uranium was found within the interstitial material, which primarily consisted of clay minerals and cementing material. Clay minerals exhibited strong adsorption capabilities with uranium being adsorbed by the clay minerals and subsequently precipitating around or within them.

5. DISCUSSION

5.1. Rock Types of Provenance. The geochemical characteristics of sandstone samples can reflect the material composition characteristics of the sediment source areas.[34,35] Some trace elements with weaker activity and ratios exhibited poor migration and minimal changes during sedimentation. Therefore, their transfer to sediment can still reflect the geochemical habits of the parent rock and can be an ideal object for identifying material sources.[36,37] REEs are generally considered nonmigratory, and the REE content in sediments is mainly constrained by the REE abundance and weathering conditions in the source rocks. Transport, sedimentation, and diagenesis had little effect on the REE content in the sediments, and the REE distribution pattern did not change significantly from the source to the sedimentary site. The REE contents of the sediments effectively reflect the characteristics of the source rocks.[30,38,39]

During the formation of sandstone, processes such as weathering, erosion, transportation, sedimentation, and later alteration occur, which inevitably affect its chemical composition. The contents of unstable elemental oxides, such as CaO, Na_2O, and K_2O, undergo significant changes owing to oxidation effects, as extensively documented in the literature.[40,41] Consequently, these oxides have been widely employed as indicators of the degree of sample weathering.[42,43] Due to K metasomatism and cyclic sedimentation, the chemical index of alteration (CIA) of the chemical weathering process, which affects the reliability of its products, can be overestimated. Therefore, an index of compositional variability (ICV) was used for correction. If ICV > 1, then fine-grained clastic rocks contain little clay material, indicating initial deposition in an active tectonic belt; and if ICV < 1, then the fine-grained clastic rocks contain a high amount of clay material, which indicates that the sediments have experienced sedimentary recycling or initial deposition under heavy weathering.[42,43] The ICV values in the study area range from 1.25 to 3.79, with an average of 1.67, all >1, indicating that the clastic rocks in the study area are in the initial sedimentary stage of the active tectonic zone. A−CN−K diagrams are often used to reflect the degree of weathering and effect of diagenesis

https://doi.org/10.1021/acsomega.3c06163
ACS Omega 2024, 9, 3324−3341

or metasomatism on samples. Heavier weathering of the provenance generally corresponds to a higher CIA value. The A−CN−K diagram (Figure 6) indicates that the effect of potassium metasomatism on the CIA of the studied samples can be neglected.[42,43] The CIA values of the Huanhe Formation samples in the study area were close to the ideal weathering trend line (Figure 6), indicating that the provenance was not affected by weak potassium metasomatism. At the same time, the K_2O contents (1.88−2.72%, avg. of 2.4%) of the samples were lower than those of the upper crust (2.80%),[44] which also indicated that the sediments in the provenance area were not affected by potassium metasomatism. Thus, the CIA can effectively determine weathering in the provenance area. The CIA values for the study area ranged from 46.27 to 53.87, with an average of 49.90. The CIA values were close to those of the continental upper crust (49.21), which indicates that sedimentary sorting had little impact on the CIA value. Therefore, the low CIA value of sandstone in the study area can reflect the general chemical weathering conditions of the source area.[45,46] Similarly, the chemical index of weathering (CIW) values varied from 51.40 to 60.29, with an average of 55.35 (Table 1), thus reflecting the relatively small impact of diagenesis and metamorphism after sedimentation on the chemical composition of rocks.

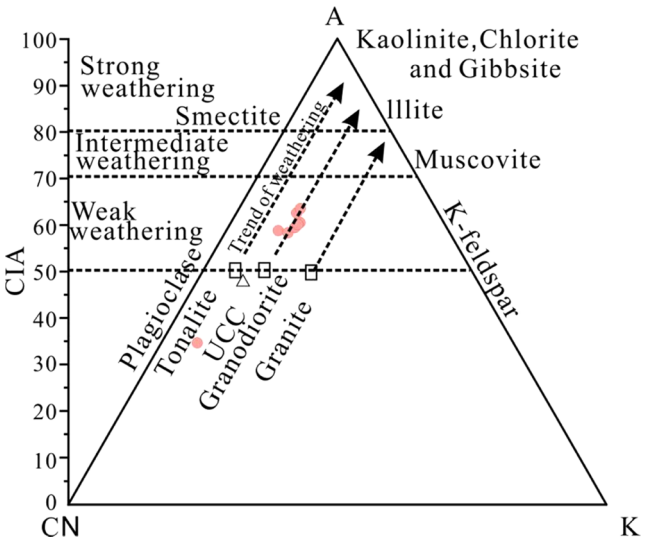

Figure 6. A−CN−K diagram of sandstone in the Huanhe Formation in the Yihewusu area of the Ordos Basin.[47] Adapted with permission from ref 47. Copyright: [Geochimica et Cosmochimica Acta, 1984].

The major elements can serve as criteria for classifying sedimentary rocks and assessing their compositional maturity. The SiO_2 content was primarily controlled by the quartz content, whereas the Al_2O_3 content reflected the presence of clay minerals and feldspar. The SiO_2/Al_2O_3 ratio can be used as an indicator of compositional maturity.[48] In this study, the SiO_2/Al_2O_3 ratios of the samples ranged from 5.26 to 6.07, with an average of 5.66. This value fell within the range of SiO_2/Al_2O_3 values (>5) typical of mature sedimentary rocks,[49]

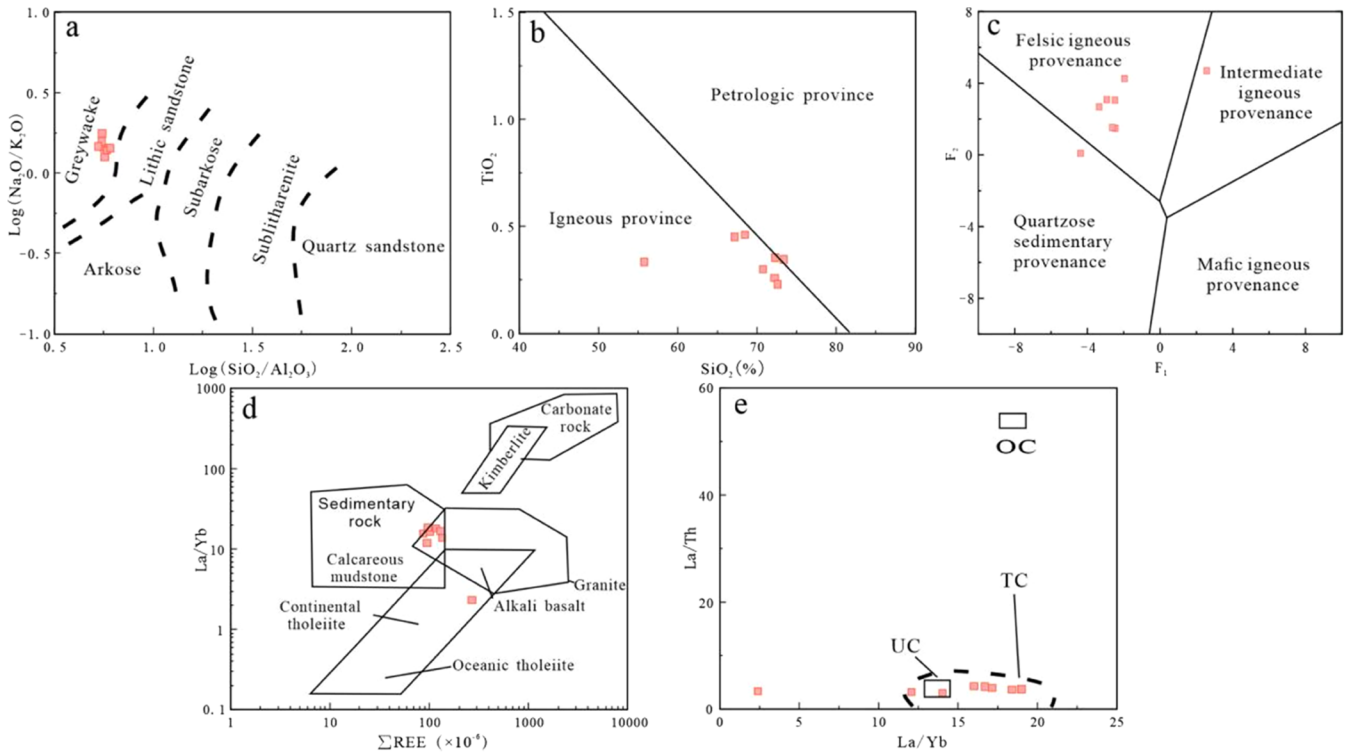

Figure 7. Diagram for distinguishing the source rock types of sandstones from the Huanhe Formation in the Yihewusu area, Ordos Basin. (a) $lg(Na_2O/K_2O)$-$lg(SiO_2/Al_2O_3)$ (from Pettijohn et al.[51]); (b) TiO_2−SiO_2 (from Roser and Korsch[52]); (c) F_2−F_1 (from Roser and Korsch[52]); (d) La/Yb-∑REE (from Bhatia[36]); and (e) La/Th−La/Yb (from Shao and Stattegger[53]). $F_1 = -1.773 \times TiO_2 + 0.607 \times Al_2O_3 + 0.76 \times Fe_2O_3 - 1.5 \times MgO + 0.616 \times CaO + 0.509 \times Na_2O - 1.224 \times K_2O - 9.090$ and $F_2 = 0.445 \times TiO_2 + 0.07 \times Al_2O_3 - 0.25 \times Fe_2O_3 - 1.142 \times MgO + 0.438 \times CaO + 1.475 \times Na_2O + 1.426 \times K_2O - 6.8610$. (a) Adapted from ref 51 Copyright: [New York: Springer-Verlag, 1972]. (b, c) Adapted with permission from ref 52. Copyright: [The Journal of Geology,1986]. (d) Adapted with permission from ref 36. Copyright: [Sedimentary Geology,1985]. (e) Adapted from ref 53. Copyright: [Journal of Sedimentary Research. 2001].

https://doi.org/10.1021/acsomega.3c06163
ACS Omega 2024, 9, 3324−3341

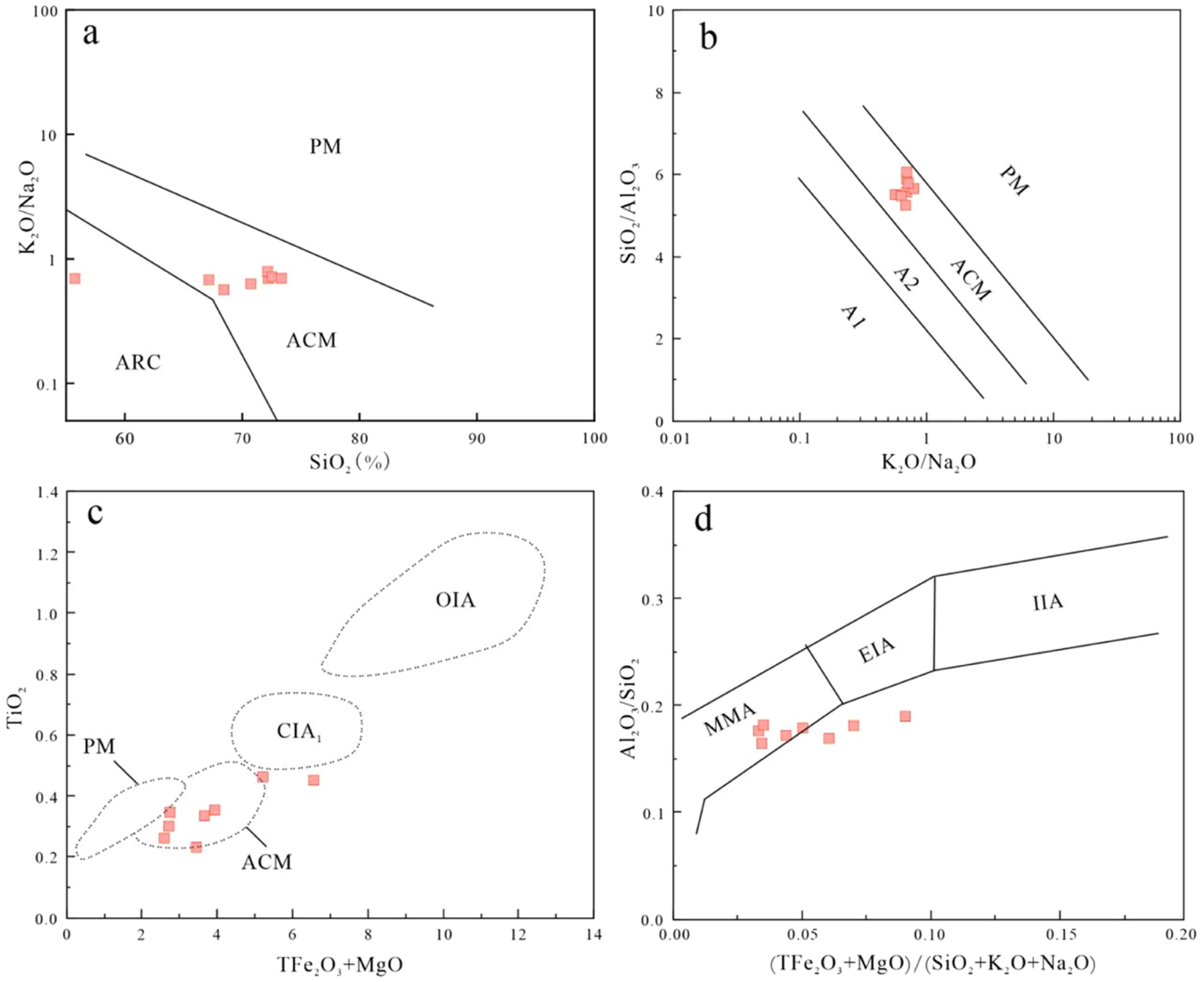

Figure 8. Tectonic setting discrimination diagram of the sandstone source area of the Huanhe Formation in the Yihewusu area of the Ordos Basin. (a) K_2O/Na_2O-SiO_2 (from Roser and Korsch[52]); (b) SiO_2/Al_2O_3−K_2O/Na_2O (from Maynard et al.[57]); (c) TiO_2−(TFe_2O_3 + MgO) (from Bhatia[54]); and (d) Al_2O_3/SiO_2-(TFe_2O_3 + MgO)/(SiO_2 + K_2O + Na_2O) (from Kumon and Kiminami[55]). PM, passive margin; ACM, active continental margin; ARC, oceanic island arc margin; A1, arc setting, basaltic, and andesitic detritus; A2, evolved arc setting, felsitic−plutonic detritus; OIA, oceanic island arc; CIA_1, continental island arc; IIA, immature island arc; EIA, evolved island arc; MMA, mature magmatic arc. (a) Adapted with permission from ref 52. Copyright: [The Journal of Geology, 1986]. (b) Adapted with permission from ref 57. Copyright: [Geological Society, 1982]; (c) Adapted with permission from ref 54. Copyright: [The Journal of Geology, 1983]; (d) Adapted with permission from ref 55. Copyright: [Proceedings 29th IGC, 1994].

indicating the relatively mature nature of the sandstone in the Huanhe Formation. The petrographic characteristics reflected a similar proportion of debris and rock debris. The findings in Figure 7a comprehensively reveal that the sandstone of the Huanhe Formation in the Ordos Basin is mainly composed of greywacke.

In the TiO_2−SiO_2 diagram, the sample points are situated in the transitional region between igneous rocks and the boundary between igneous and sedimentary rocks (Figure 7b), thus indicating a predominant contribution from igneous source rocks with minor input from sedimentary sources. Roser and Korsch[50] established discriminant functions (F_1 and F_2) to differentiate source rock types based on the oxide contents of Ti, Al, Fe, Mg, Ca, Na, and K in the sediments. By utilizing the F_2−F_1 plot, it was possible to effectively distinguish magnesian, intermediate, and felsic igneous rocks from quartz-rich sedimentary rocks as potential source rocks. In the F_2−F_1 plot, the majority of samples fell predominantly within the felsic igneous source area, with a few samples positioned in transitional zones between the felsic igneous source and neutral igneous source, as well as between the felsic igneous source and quartz-rich sedimentary source regions (Figure 7c).

In the La/Yb-∑REE diagram, sample points predominantly clustered in the overlapping region among sedimentary rocks, calcareous mudstone, and granitic compositions with only one sample positioned within the basaltic area (Figure 7d). In the La/Th−La/Yb diagram, the sample points were primarily situated near the average upper continental crust values (Figure 7e). These characteristics collectively indicate that the provenance of the Huanhe Formation sandstone in the

https://doi.org/10.1021/acsomega.3c06163
ACS Omega 2024, 9, 3324−3341

Table 5. Characteristic Parameters of the Trace Element Sedimentary Environment of the Sandstone from the Huanhe Formation in the Yihewusu Area of the Ordos Basin

F.m	type	sample no.	lithology	Sr/Ba	Sr/Cu	V/Cr	U/Th	UCC-Mo_{EF}	UCC-U_{EF}	PAAS-Mo_{EF}	PAAS-U_{EF}
K_1h	nonore-bearing sandstone	ER2020-17	gray medium sandstone	0.46	15.78	3.50	11.58	0.11	2.32	0.22	2.62
		ER2020-14	green medium sandstone	0.68	44.70	1.95	5.55	0.29	1.88	0.55	2.12
		ER2020-19	brownish-red medium sandstone	0.48	40.15	1.42	0.68	0.15	0.16	0.29	0.19
	ore-bearing sandstone	ER2020-12	brownish-red coarse sandstone	0.27	15.78	4.40	130.83	0.67	32.27	1.27	36.43
		ER2020-22	gray fine sandstone	0.82	30.65	9.90	126.36	8.32	45.76	15.80	51.66
		ER2020-8	brownish-red coarse sandstone	0.41	38.28	6.61	114.01	26.83	35.46	50.97	40.04
	nonore-bearing sandstone	ER2020-6	green coarse sandstone	0.41	39.28	1.34	2.07	0.13	0.58	0.24	0.65
		ER2020-5	gray calcareous fine sandstone	0.54	44.20	1.09	0.41	0.13	0.17	0.25	0.19

study area is primarily attributed to felsic igneous rocks originating from the continental upper crust.

The REE composition of the North American Shale Composite (NASC) is commonly employed to represent the REE characteristics of upper crustal compositions.[38] In the NASC-normalized REE distribution diagram for sedimentary rocks in the study area, the normalized curves exhibited a near-horizontal distribution (Figure 4b), suggesting similarities in REE composition with the NASC and implying that the Huanhe Formation sandstone primarily originated from the continental upper crust. The chondrite-normalized distribution pattern (Figure 4a) indicated a consistent trend in the distribution curves of the Huanhe Formation sandstone, which is similar to the upper crustal composition. This finding further indicates that the source rocks originated primarily from the continental upper crust.

5.2. Tectonic Setting. Bhatia[54] categorized continental margins and ocean basins into four tectonic types: oceanic island arcs, continental island arcs, active continental margins, and passive continental margins. Bhatia also proposed major element geochemical parameters for discriminating sedimentary basin tectonic settings as well as multivariate tectonic setting discrimination diagrams and bivariate diagrams. In the SiO_2-(K_2O/Na_2O) diagram (Figure 8a), the sandstone samples of the Huanhe Formation predominantly fall within the active continental margin field, with only a few projecting into the island arc domain. In the (K_2O/Na_2O)−(SiO_2/Al_2O_3) diagram (Figure 8b), the sandstone samples from the study area are situated in the active continental margin region. In the (TFe_2O_3 + Mg)−TiO_2 diagram (Figure 8c), most of the samples were positioned within the active continental margin field, with a small portion intersecting the boundary between the active continental margin and continental island arc as well as the boundary between the active continental margin and passive continental margin and predominantly aligning with the active continental margin domain.

Kumon and Kiminami[55] proposed the use of the (Al_2O_3/SiO_2)−(TFe_2O_3 + MgO)/(SiO_2 + K_2O + Na_2O) diagram to differentiate between immature island arcs, evolved island arcs, and mature magmatic arcs. In this context, Al_2O_3/SiO_2 roughly signifies the proportion of feldspar to quartz, whereas (TFe_2O_3 + MgO)/(SiO_2 + K_2O + Na_2O) represents the ratio of relatively basic components to felsic components.[56] In this diagram (Figure 8d), the majority of samples fell within the mature magmatic arc field. A comprehensive analysis indicated that the tectonic setting of the provenance region corresponds to an active continental margin.

The Ordos Basin is situated in a complex superimposed region with multiple tectonic domains. The evolutionary processes and geodynamic settings are highly intricate. The potential source areas surrounding the study region primarily include the Yin Mountains, Daqing-Wula Mountains, Jining area, Lang Mountains, Helan Mountains, Zhuozi Mountains, and eastern edge of Alxa.[16] The Huanhe Formation sandstones in the Ordos Basin encompass four major age groups: 235−330, 390−455, 1700−1980, and 2370−2540 Ma.[58] The peak age of 235−330 Ma coincides with the ages of the intrusive rock bodies in the northern part of the study area, including the Daqing Mountains, Wulate Zhongqi, Guyang, Siziwangqi, and Baiyunebo, and the eastern edge of Alxa in the west. For instance, the Xiaojingou granite body in the Daqing Mountains has an age of 275 ± 1 Ma.[59] In the Wulate Zhongqi region, the Wuliangstai granite has an age of 277 ± 3 Ma,[16,60] and the De'ersi granite body has an age of 279 ± 3 Ma.[16,61] In the Guyang region, the adakite granite body has an age of 281.9 ± 3.1 Ma.[16,62] In the Siziwangqi region, there are granites with ages of 264 ± 3.4 and 266 ± 2 Ma.[16] The Baiyunebo area features a peak age of 269 Ma for granodioritic−granitic intrusions.[16,63] In the Alxa Desert region, weakly deformed granites from the Early Permian are widely distributed, and they are concentrated in the age range of 269−289 Ma.[17] The peak age of 2370−2540 Ma corresponds to the ages of granite bodies in the Daqing-Wula Mountains in the northern part of the study area. For instance, in the Daqing Mountains region, Early Paleoproterozoic biotite granite with an age of 2430 ± 19 Ma is observed, while in the Ula Mountains region, Zisu granite with an age of 2430 ± 7.7 Ma is observed.[16] Combining the geochemical characteristics of sandstone elements in the study area and the evidence obtained from detrital zircon geochronology, it is suggested that the predominant sources of detrital rock in the study area are likely intermediate-acidic intrusive rocks exposed in the Daqing Mountains, Ula Mountains, Yin Mountains, and the eastern margin of the Alxa. The presence of abundant granite clasts in the Huanhe Formation sandstone (Figure 3c) further supports this hypothesis.

5.3. Sedimentary Environment. Since the Late Mesozoic, most regions in China have undergone continental sedimentation during which continental strata directly interacted with the atmosphere. Paleoenvironmental and paleoclimatic characteristics and changes during the sedimen-

https://doi.org/10.1021/acsomega.3c06163
ACS Omega 2024, 9, 3324−3341

tation period have been keenly recorded.[64−66] Some redox-sensitive trace elements in sedimentary rocks, such as Ba, Cu, V, Cr, and U, exhibit variable valence states that are influenced by environmental changes. The redox conditions of the environment control the enrichment of trace elements in sediments. As a result, these redox-sensitive elements can indicate the depositional environment of sedimentary rocks, and their mass fractions and element ratios are crucial indicators for interpreting the sedimentary environments.[65,67,68] Therefore, in this study, the trace element characteristic ratios in the sandstone samples from the Lower Cretaceous Huanhe Formation in the northwestern Ordos Basin were analyzed (Table 5). By utilizing indicators such as the Sr/Ba, Sr/Cu, V/Cr, and U/Th ratios of trace elements in sandstones, the evolutionary patterns of sedimentary environments in the northwestern part of the Ordos Basin were revealed.[69−72]

(1) The Sr/Ba ratio is frequently used as an indicator of the salinity of sedimentary water bodies. A Sr/Ba ratio greater than 0.5 indicates a marine water environment, a ratio between 0.2 and 0.5 indicates a brackish water environment, and a ratio less than 0.2 suggests a freshwater environment.[65,67] In the studied Huanhe Formation sandstones, the Sr/Ba ratios ranged from 0.27 to 0.82. Most of them were between 0.2 and 0.5, with a small portion exceeding 0.5. These findings indicated that the Huanhe Formation developed brackish-to-marine water environments. This suggests that the depositional environment of the Huanhe Formation in the northwestern part of the Ordos Basin was characterized by brackish-to-marine water conditions.

(2) The V/Cr ratio is commonly employed as a significant indicator of redox conditions. A V/Cr ratio < 2 indicates an oxygenated environment, a ratio between 2.00 and 4.25 indicates a suboxic environment, and a ratio > 4.25 indicates a suboxic to anoxic environment.[65,67] In the studied Huanhe Formation sandstone, the V/Cr ratios range from 1.09 to 9.90. For samples ER20-12, ER20-22, and ER20-8, which represent uranium-bearing minerals, the V/Cr values were all >4.25, suggesting that these mineral-bearing sandstones were deposited in an anoxic environment. In contrast, sample ER20-17, which exhibited slightly enriched uranium content, had a V/Cr ratio of 3.50, indicating a suboxic environment. The V/Cr values of the other nonore-bearing sandstone samples were close to 2, indicating mildly oxygenated conditions. This implies that the oxygen content gradually decreased during uranium enrichment in the Huanhe Formation sandstones, further suggesting the occurrence of redox reactions during mineralization.

(3) The U/Th ratio is commonly used as an indicator to discern the redox conditions of water bodies. It is generally accepted that U/Th ratios > 1.25 indicate an anoxic environment, ratios from 0.75 to 1.25 indicate a suboxic environment, and ratios < 0.75 indicate an oxidizing environment.[65,67] The U/Th values for most of the nonore-bearing sandstones were greater than 1.25, indicating that the nonore-bearing sandstones were in a hypoxic environment. The U/Th values of the Huanhe Formation sandstones in the study area showed a positive correlation with uranium content. This suggests that the oxygen content gradually decreased during uranium enrichment in the sandstones, further implying the occurrence of redox reactions during mineralization.

(4) Mo and U elements are found in very low concentrations in phytoplankton, and their sedimentary enrichment is generally derived from autogenic enrichment. In oxidized seawater, Mo exists in the form of stable and inactive molybdate ions (MoO_4^{2-}). Given the very limited accumulation of authigenic Mo in an oxidized environment, the concentration of seabed sediments in the modern continental rim is as low as 1−5 ppm.[73−75] Under anoxic sulfur-rich conditions, a specific concentration of hydrogen sulfide (approximately 50−250 μM) is capable of activating Mo, thereby catalyzing the conversion of molybdate into thiomolybdate ($MoO_xS_{(4-x)}^{2-}$, x = 0−3),[70,71,73,76] and the latter is easily deposited with sulfurized organic matter or iron sulfides.[77−80] Under oxidized conditions, U primarily occurs in the form of soluble hexavalent uranyl carbonate complexes and shows chemical inertness.[81−85] The enrichment of authigenic U is relatively limited in an oxidizing environment, and the U concentrations are only 1−5 ppm in seabed sediments of the modern continental rim.[30,86,87] Under anoxic conditions, hexavalent U(VI) is reduced into tetravalent U(IV) in the possible form of insoluble uranyl ions UO^{2+} or weakly soluble uranyl fluoride complexes. Therefore, the above chemical properties of Mo and U show that these elements can be used to evaluate the redox conditions of ancient waters. Studies before 2000 mainly analyzed the original concentrations and the ratios between these two elements,[72] while recent studies tend to use the standardized enrichment coefficient of Al to evaluate the redox conditions of ancient waters 86−88. The formula for calculating the enrichment coefficient is given as follows

$$\mathrm{XEF} = (\mathrm{X/Al})\ \mathrm{sample}/(\mathrm{X/Al})\ \mathrm{UCC\ or\ PAAS}$$

where X and Al represent the mass concentrations of elements X and Al (ppm), respectively. The samples are generally standardized using upper continental crust (UCC) rocks[38] or post-Archean average shales (PAAS) from Australia.[30] U/Al_{UCC} has a value of 0.35×10^{-4} and Mo/Al_{UCC} has a value of 0.19×10^{-4}; and U/Al_{PAAS} and Mo/Al_{PAAS} have values of 0.31×10^{-4} and 0.10×10^{-4}, respectively.[72] An element has good autogenetic enrichment if its enrichment coefficient is greater than 3 and less than 10 or large-scale autogenetic enrichment if its enrichment coefficient is greater than 10.

According to the contents of Mo and U in the sandstone samples of the Huanhe Formation in the Yihewusu area of the Ordos Basin, the enrichment coefficients of Mo and U were calculated using UCC and PAAS of Australia. The Mo_{EF} and U_{EF} values of UCC and PAAS in the Huanhe Formation ore-bearing sandstone are much lower than those in nonore-bearing sandstone. This indicates that the redox conditions of the ancient water bodies in the Huanhe Formation were lower in terms of oxidation in ore-bearing sandstones than in nonore-bearing sandstones. Therefore, ore-bearing sandstone was in a reducing environment, while nonore-bearing sandstone was in an oxidizing environment relative to ore-bearing sandstone.

According to the compiled database of modern marine systems, Mo concentrations below 25 ppm usually represent a noneuxinic environment, those between 25 and 100 ppm

https://doi.org/10.1021/acsomega.3c06163
ACS Omega 2024, 9, 3324−3341

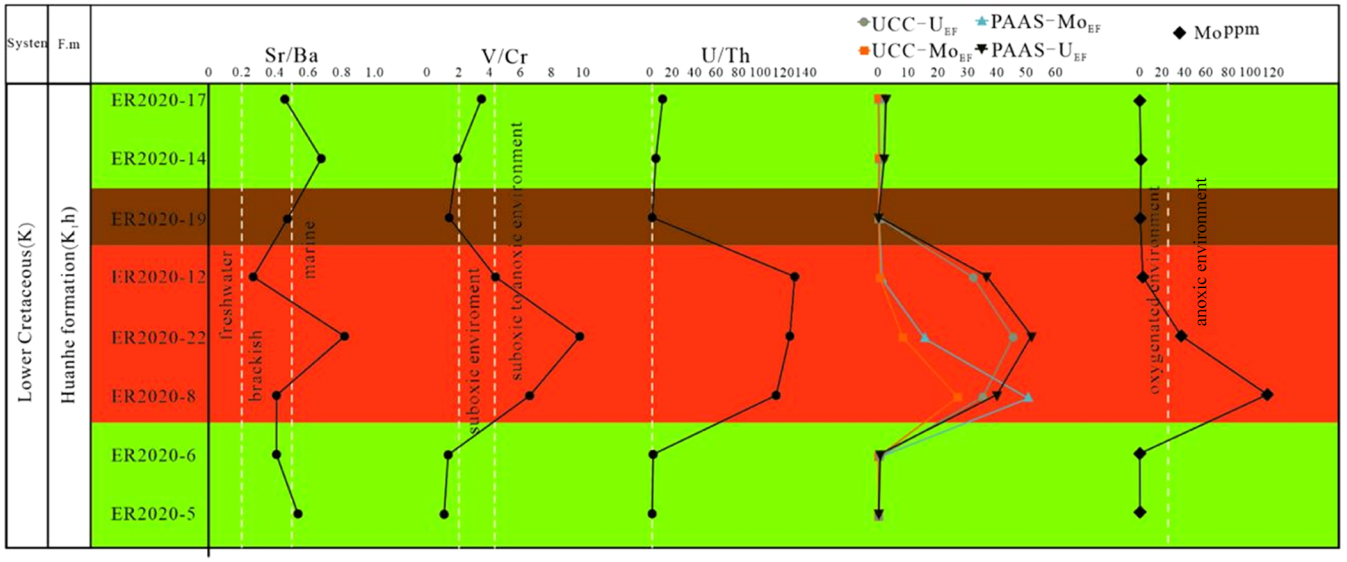

Figure 9. Sedimentary Environment Evolution of the Yihewusu Huanhe Formation in the Ordos Basin.

usually represent intermittent euxinia, and those greater than 100 ppm usually represent persistent euxinia.[88−91] The Mo_{EF} and U_{EF} values of the ore-bearing sandstone in the Huanhe Formation were generally greater than 25, while the Mo_{EF} and U_{EF} values of the nonore-bearing sandstone were all less than 25. This also indicates that the ore-bearing sandstone was in a reducing environment, while the nonore-bearing sandstone was in an oxidizing environment.

In summary, analysis of the trace element ratios (Sr/Ba, V/Cr, U/Th, Mo_{EF}, and U_{EF}) of the Lower Cretaceous Huanhe Formation sandstones in the northwestern part of the Ordos Basin clearly showed that the sedimentary environment of the Huanhe Formation experienced significant fluctuations (Figure 9). Overall, the environment was a freshwater to brackish environment. The ore-bearing layers (ER2020-12, ER2020-22, ER2022-8) belonged to a reducing environment, whereas the nonore-bearing layers belonged to a weakly oxidizing environment.

5.4. Uranium Mineralization and Mineralization Models. Previous studies have indicated that rocks surrounding sandstone-type uranium deposits can serve as significant sources of ore-forming materials. The contribution of these host rocks to uranium mineralization depends directly on the active uranium content in the source rocks. Therefore, host rocks with higher uranium concentrations are favorable for initial enrichment.[27,92] In the northern part of the basin, there are three major granite plutons with well-exposed outcrops: the Langshan Granite Pluton, Daqing Mountain Granite Pluton, and Yinshan Granite Pluton. The Langshan Granite Pluton consists of nearly a hundred different-sized plutons with widely distributed deposition times, primarily during the Variscan Period. These plutons belong to central Inner Mongolia granite. Previous research suggested that the granite plutons deposited during the Variscan period had a uranium content of 7.8×10^{-6}, and multiple uranium mineralization events have been identified within these plutons.[93,94] The Daqing Mountain Granite Pluton has an overall higher uranium content ($4-8 \times 10^{-6}$), indicating that it has a uranium-enriched structure.[93,94] Scholars have identified an average Th/U ratio of 4.2 for mainland Chinese rocks. A Th/U ratio greater than 4.2 is considered indicative of significant uranium loss in rocks.[68] Moreover, the Th/U ratio in this region was 48.8, indicating a considerable migration of uranium from uranium-enriched granite plutons in the source area. Thus, these plutons represented abundant uranium sources for the Yihewusu area. Furthermore, the sand bodies of the Huanhe Formation in the study area exhibit a relatively high whole-rock uranium content ($2.64-48.3 \times 10^{-6}$). This suggests that during the weathering and erosion processes, uranium-bearing debris from the source rocks was transported by surface water and other media and accumulated in the Yihewusu area, where it accumulated.[95] In humid paleoclimate and sedimentary environments characterized by rapid near-source deposition, sandstones contain significant amounts of pyrite framboids and minor amounts of carbonaceous organic matter, both of which are reducing substances.[27,96] During the early burial stage, the sandstones remained in a reducing environment, thus preserving the uranium-bearing debris. This further contributed to the preenrichment of uranium in the sandstones of the Huanhe Formation.

In the natural environment, uranium mainly exists in three forms: discrete uranium minerals (such as uraninite, pitchblende, and coffinite), as isomorphous analogues (uranium-bearing secondary minerals, such as zircon and monazite), and dispersed adsorption (often adsorbed onto coal seams and clay minerals).[97,98] Under oxidizing conditions, uranium exists in the hexavalent state (U^{6+}) and migrates in the form of uranyl carbonate, uranyl phosphate, or uranyl fluoride complexes. Under reducing conditions, uranium precipitates in the tetravalent state (U^{4+}) to form uranium minerals such as pitchblende, uraninite, and coffinite.[99−102] During the Jurassic to Cretaceous era, extensive coal-bearing and oil-bearing rock formations were deposited in the northern continental basins, forming a characteristic red-black rock series. This red-black rock series is the main ore-bearing stratum for sandstone-type uranium deposits in the northern region. The coexistence of the black and red rock series in Mesozoic continental basins represents a transition from a reducing to an oxidizing paleoenvironment. The red layers formed under oxidizing conditions provide a site for the dissolution of uranium minerals by surface fluids, while the black rock series acts as a barrier for uranium mineral

https://doi.org/10.1021/acsomega.3c06163
ACS Omega 2024, 9, 3324−3341

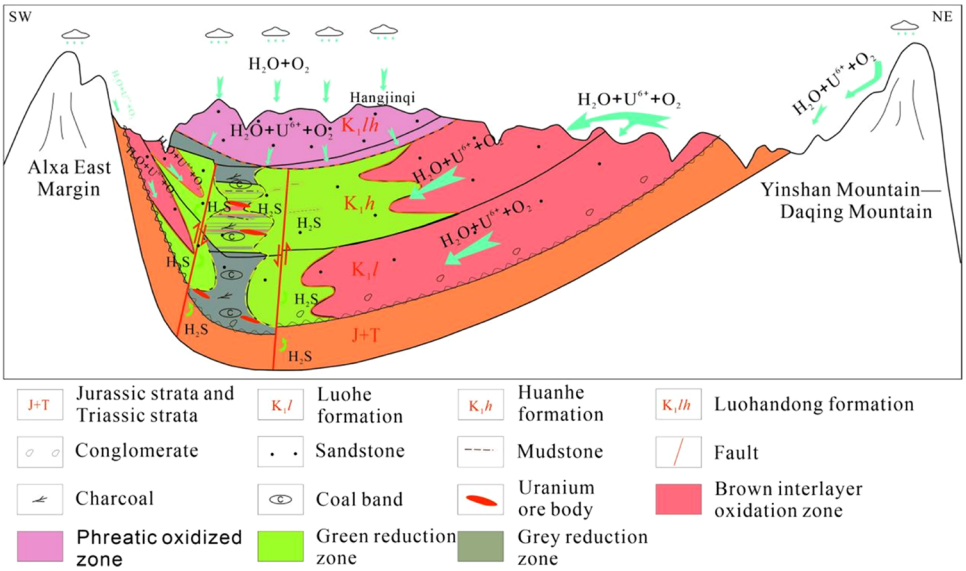

Figure 10. Uranium mineralization model map of the Yihewusu Huanhe Formation in the Ordos Basin. (Revised by Wang et al.[19]) Adapted with permission from ref 19. Copyright: [Bulletin of Geological Science and Technology, 2023].

precipitation. This interplay between the red-black rock series indicates a close spatial and temporal association between sandstone-type uranium deposits and the "red-black rock series" in the northern continental basins.[103−105] The Ordos Basin is an important area for exploring coal, oil, and gas resources. With later intensified tectonic activity, deep-seated reducing fluids escaped and infiltrated the strata. Additionally, the abundant presence of pyrite framboids and organic matter in the form of coal served as reducing agents, thereby facilitating uranium mineralization within the region. From the Late Cretaceous to the Early Eocene, the basin experienced regional uplift and limited sediment deposition, resulting in prolonged periods of exposure for Triassic, Jurassic, and Lower Cretaceous formations. The arid climate during this period favored the development of the oxidation processes. Eventually, uranium-rich fluids originating from source areas, including uranium-bearing groundwater and atmospheric precipitation, vertically penetrated the ore-bearing sandstone bodies. These uranium-enriched fluids continuously generate free $[UO_2]^{2+}$ ions. When the concentration of $[UO_2]^{2+}$ ions reached saturation, the reducing agents present in the Yihewusu region (including reducing gases such as CH_4 and H_2S, coal seams, sulfides, and pyrite) led to the occurrence of redox reactions. U^{6+} ions were reduced to U^{4+} ions, which precipitated as independent uranium minerals, such as coffinite and pitchblende, within the region (Figure 10).[106]

6. CONCLUSIONS

(1) This study revealed for the first time that the independent uranium minerals in the Yihewusu area of Hangjin Banner are mainly coffinite, which is commonly found in association with detrital grains, along the edges or concavities of pyrite framboids, and within cleavage fissures of biotite. Previous reports have only provided data for the Dongsheng area in the eastern part of the study area.

(2) By combining the analysis of sandstone trace element ratios, such as Sr/Ba, V/Cr, U/Th, Mo_{EF}, and U_{EF}, this research demonstrates significant fluctuations in the sedimentary environment of the ore-bearing strata within the Huanhe Formation. Overall, these strata suggest a brackish-to-marine water setting. The ore-bearing layers correspond to reducing conditions, whereas the nonore-bearing layers indicate weakly oxidizing conditions.

(3) The integrated analysis of sandstone detrital components and elemental geochemical characteristics indicates that the Huanhe Formation sandstone in the Yihewusu region originated primarily from a tectonic setting along an active continental margin. The main sources of sediment were medium-acidic intrusive rocks exposed in the northern part of the basin, including the Daqing-Wula Mountain region, Yin Mountains, and eastern edge of Alxa in the western part of the basin.

(4) A comparison of the uranium contents and Th/U ratios in the Variscan period granitic rocks from the source region revealed that the predominant contribution of uranium-enriched granitic rocks from the source region led to the preenrichment of uranium in the targeted uranium-bearing sandstone layers. Ultimately, this uranium precipitated as an ore through redox reactions.

■ ASSOCIATED CONTENT

Data Availability Statement

All data generated or analyzed during this study are included in this article.

■ AUTHOR INFORMATION

Corresponding Authors

Da Sun − *School of Earth Sciences, East China University of Technology, Nanchang 330013 Jiangxi, China; State Key Laboratory of Nuclear Resources and Environment, East China University of Technology, Nanchang 330013 Jiangxi, China;* orcid.org/0009-0006-4153-9880; Email: 630389762@qq.com

Huaming Li − *Geological Party No. 208, CNNC, Baotou 014010 Inner Mongolia, China*; Email: 877150769@qq.com

https://doi.org/10.1021/acsomega.3c06163
ACS Omega 2024, 9, 3324−3341

Fei Xia − *School of Earth Sciences, East China University of Technology, Nanchang 330013 Jiangxi, China; State Key Laboratory of Nuclear Resources and Environment, East China University of Technology, Nanchang 330013 Jiangxi, China*; Email: fxia@ecut.edu.cn

Authors

Fengjun Nie − *School of Earth Sciences, East China University of Technology, Nanchang 330013 Jiangxi, China; State Key Laboratory of Nuclear Resources and Environment, East China University of Technology, Nanchang 330013 Jiangxi, China*

Guangwen Huang − *College of Emergency and Disaster Reduction, Qinghai Normal University, Xining 810008 Qinghai, China*

Zhibo Zhang − *School of Resources and Geosciences, China University of Mining and Technology, Xuzhou 221116, China*; orcid.org/0000-0002-7140-1253

Fanmin Meng − *School of Earth Sciences, East China University of Technology, Nanchang 330013 Jiangxi, China; State Key Laboratory of Nuclear Resources and Environment, East China University of Technology, Nanchang 330013 Jiangxi, China*

Jiayong Pan − *School of Earth Sciences, East China University of Technology, Nanchang 330013 Jiangxi, China; State Key Laboratory of Nuclear Resources and Environment, East China University of Technology, Nanchang 330013 Jiangxi, China*

Yujie Hu − *Geological Party No. 208, CNNC, Baotou 014010 Inner Mongolia, China*

Complete contact information is available at: https://pubs.acs.org/10.1021/acsomega.3c06163

Funding

National Natural Science Foundation of China Project—Study on the Formation Conditions of Fe−Ti−U Minerals and Uranium Metallogenesis Mechanism in Qianjiadian-Baolongshan Uranium Deposit, Kailu Basin (Project Number 42172098); Joint Innovation Fund Project between the State Key Laboratory of Nuclear Resources and Environment, East China University of Technology, and China Uranium Corporation—Study on Uranium and Associated Rhenium Element Migration and Enrichment Mechanism in Sandstone-type Uranium Deposit, Kailu Basin (Project Number NRE2021-15); Joint Innovation Fund Project between the State Key Laboratory of Nuclear Resources and Environment, East China University of Technology, and China Uranium Corporation—Study on Hyperenrichment Mechanism and Prospecting Prospects of Sandstone-type Uranium Deposits in Cretaceous of Ordos Basin (Funding Number NRE2021-02); Mechanism of Basin−Mountain Coupling Process Controlling Uranium Mineralization in the Southern and Two-sided Basins of Daxing'anling Mountains (Funding Number U2244205); and East China University of Technology Graduate Innovation Project—Mineralogical characteristics and source tracing of the Lower Cretaceous sandstone-type uranium deposit in the northwest of the Ordos Basin (Funding Number DHYC-202306).

Notes

The authors declare no competing financial interest.

REFERENCES

(1) Li, Z. Y. *Sandstone-Hosted Uranium Metallogeny in North Ordos Basin, China*; Geological Publishing House: Beijing, 2019; pp 4−50.

(2) Zhu, Q.; Li, J. G.; Wen, S. B.; Li, G. Y.; Yu, R. G.; Miao, P. S.; Zhang, B. Alteration, uranium occurrence state, and enrichment mechanism of the Cretaceous Luohe Formation, southwestern Ordos Basin, western China. *Ore Geol. Rev.* **2021**, *139*, No. 104496.

(3) Chen, Y.; Miao, P. S.; Li, J. G.; Jin, R. S.; Zhao, H. L.; Chen, L. L.; Wang, C.; Yu, H. Y.; Zhang, X. R. Association of Sandstone-Type Uranium Mineralization in the Northern China with Tectonic Movements and Hydrocarbons. *J. Earth Sci.* **2022**, *33* (2), 289−307.

(4) Ejeh, O. I.; Abiodun, A. I. E.; Edwin, O. A. Pattern of Geochemical and Sedimentological Variability of the Albian toCenomanian Upper Bima Sandstone, Benue Trough, Nigeria: Implications on Tectonic provenance and Source Area Weathering. *J. Environ. Sci.* **2013**, *3*, 170−184.

(5) Ikhane, R.; Akintola, A. I.; Bankole, S. I.; Oyinboade, Y. T. Provenance Studies of Sandstone Facies Exposed Near Igbile Southwestern Nigeria: Petrographic and Geochemical Approach. *J. Geogr. Geol.* **2014**, *6*, 47−68.

(6) Khan, T.; Sarma, D. S.; Somasekhar, V.; Ramanaiah, S.; Reddy, N. R. Geochemistry of the Palaeoproterozoic quartzites of LowerCuddapah Supergroup, South India: Implications for the palaeoweathering, provenance, and crustal evolution. *Geol. J.* **2020**, *55*, 1587−1611.

(7) Khan, T.; Sarma, D. S.; Khan, M. S. Geochemical study of the Neoproterozoic clastic sedimentary rocks of the Khambal Formation-(Sindreth Basin), Aravalli Craton, NW Indian Shield: Implications for paleoweathering, provenance, and geodynamic evolution. *Geochemistry* **2020**, *80*, No. 129956.

(8) Wanas, H. A.; Assal, E. M. Provenance, tectonic setting and source area-paleoweathering of sandstones of the Bahariya Formationin the Bahariya Oasis, Egypt: An implication to paleoclimate and paleogeography of the southern Neo-Tethys region duringEarly Cenomanian. *Sediment. Geol.* **2021**, *413*, No. 105822.

(9) Weltje, G. J.; Eynatten, H. Quantitative provenance analysis of sediments: review and outlook. *Sediment. Geol.* **2004**, *171*, 1−11.

(10) Li, Z.; Peng, S. T. U-Pb geochronological records and provenance system analysis of the Mesozoic-Cenozoic sandstone detrital zircons in the northern and southern piedmonts of Tianshan, Northwest China: Responses to intracontinental basin- range evolution. *Acta Pet. Sin.* **2013**, *29* (3), 739−755.

(11) Zhang, X. L.; Gao, Z. Q.; Fan, T. L.; Xue, J. Q.; Li, W. H.; Zhang, H.; Cao, F. D. Element geochemical characteristics, provenanceattributes, and paleosedimentary environment of the Paleogene strata in the Lenghu area, northwestern Qaidam Basin. *J. Pet. Sci. Eng.* **2020**, *195*, No. 107750.

(12) Li, Y.; Nie, F. J.; Jia, L. C.; Lu, S. J.; Yan, Z. B. Geochemical Characteristics, Palaeoenvironment and Provenance of Uranium-BearingSandstone in the Sifangtai Formation, Northern Songliao Basin, Northeast China. *Minerals* **2021**, *11*, 1019.

(13) Huang, G. W.; Pan, J. Y.; Xia, F.; Yan, J.; Zhang, C. Y.; Wu, D. H.; Liu, Y. Provenance of uranium mineralization of the Yuqia area, Northwest China: Constraints from detrital zircon U-Pb geochronology and Hf isotopes. *J. Earth Sci.* **2022**, *33* (6), 1549−1570.

(14) Huang, G. W.; Wu, D. H.; Huang, G. N.; Xue, W. W.; Min, Z.; Fan, P. F. Provenance of Jurassic sediments from Yuqia sandstone-type uranium deposits in the Northern margin of Qaidam Basin, China and its implications for uranium mineralization. *Minerals* **2022**, *12*, 82.

(15) Patra, A.; Shukla, A. D. Geochemical signatures of Late Paleocene sandstones from the Sanu Formation, Jaisalmer basin, westernIndia: Implication for provenance, weathering and tectonic setting. *J. Earth Syst. Sci.* **2020**, *129*, 81−92.

(16) Lei, K.; Liu, C. Y.; Zhang, L.; Wu, B. L.; Wang, J. Q.; Cun, X. N.; Sun, l. Detrital Zircon U-Pb Dating of Middle Late Mesozoic Strata in the Northern Ordos Basin: Implications for Tracing Sediment Sources. *Acta Geol. Sin.* **2017**, *91* (07), 1522−1541.

(17) Zhao, H. G.; Liu, C. Y.; Wang, H. R.; Gao, S. H.; Li, M.; Zhuo, Y. Z.; Qiao, J. X.; Zhang, S. X. Q.; Jiang, S. LA-ICP-MS detrital zircon dating and its provenance significance in Yan'an Formation of the Early-Middle Jurassic in the northwestern margin of Ordos Basin. *Earth Sci. Front.* **2015**, *22* (3), 184−193.
(18) Yu, R. A.; Si, Q. H.; Wang, S. B.; Zhu, Q.; Liu, X. X.; Wang, H. B.; Tang, Y. X. Geochemical Characteristics and Detrital Zircon U-Pb Ages of the Zhiluo Formation in the Shicaocun Area of the Western Ordos Basin and Implication for its Tectonic Setting and Provenance. *Geotecton. Metallog.* **2020**, *44* (04), 754−771.
(19) Wang, L. H.; Yan, P. B.; Jiao, Y. Q.; Wu, L. Q.; Zhang, Z. L.; Rong, H.; Zhang, F.; Li, Z. C.; Zong, W. H. Urinium metallogenic model of the Lower Cretaceous in the northern Ordos Basin. *Bull. Geol. Sci. Technol.* **2023**, *42* (3), 222−233.
(20) Luo, X. N.; Li, Z. Y.; Cai, Y. Q.; Yi, C.; Zhang, Z. L.; Zhang, Y. Y.; Zhang, Y. Provenance and Tectonic Setting of Lower Cretaceous Huanhe Formation Sandstones, Northwest Ordos Basin, North-Central China. *Minerals* **2021**, *11*, 1376.
(21) Peng, Y. B.; Li, Z. Y.; Fang, X. H.; Xie, Q. L. Metallogenetic characteristics of No.2081 Uranium Deposit in the north of Ordos Basin. *Acta Mineral. Sin.* **2006**, *26* (3), 349−355.
(22) Guo, Q. Y. Tectonic Evolution at the Western Margin of Ordos Basin with Respect to Metallogenesis of Sandstone Type Uranium Deposits; Thesis, China University of Geosciences: Beijing, 2010.
(23) Jin, R. S. *Metallogenic Geological Background of Sandstone Type Uranium Deposits in the Ordos Basin*; Science Press: Beijing, 2019; pp 1−287.
(24) Zhang, T. F.; Cheng, X. Y.; Wang, S. Y.; Miao, P. S.; Ao, C. Middle Jurassic - Early Cretaceous drastic paleoenvironmental changes in the Ordos Basin: Constraints on sandstone-type uranium mineralization. *Ore Geol. Rev.* **2022**, *142*, No. 104652.
(25) Liu, T. Study on Groud Deformation Mechanism and Numerical Model Prediction Research Thesis; Jilin University: Jilin, 2017.
(26) Wang, L. H.; Wang, G.; Yan, P. B. *Investigation and Evaluation of Uranium Resources in Yihewusu Area, Ordos City, Inner Mongolia*; Nuclear Industry Group: Baotou, Inner Mongolia, 2008.
(27) Jiao, Y. Q.; Wu, L. Q.; Peng, Y. B.; Rong, H.; Ji, D. M.; Miao, A. S.; Li, H. L. Sedimentary-tectontic setting of the deposition-type uranium deposits forming in the Paleo-Asian tectonic, North China. *Earth Sci. Front.* **2015**, *22* (1), 189−205, DOI: 10.13745/j.esf.2015.01.016.
(28) *General Administration of Quality Supervision, Inspection and Quarantine of the People's Republic of China. Quantitative Analysis of Silicate Minerals by Electron Probe Method; GB/T 15617* Standards Press of China: Beijing; 2002.
(29) Chen, F.; Hegner, E.; Todt, W. Zircon ages and Nd isotopic and chemical compositions of orthogneisses from the Black Forest, Germany: evidence for a Cambrian magmatic arc. *Int. J. Earth Sci.* **2000**, *88*, 791−802.
(30) Taylor, S. R.; McLennan, S. M. *The Continental Crust: Its Composition and Evolution*; Blackwell Scientific Publications: Oxford, 1985; pp 1−312.
(31) Feng, L. J.; Chu, X. L.; Zhang, Q. R.; Zhang, T. G. CIA (Chemical index of altera) and its applications in the Neoproterozoic Clastic rocks. *Earth Sci. Front.* **2003**, *10* (04), 539−544.
(32) Yang, J. H.; Du, Y. S.; Xu, Y. J.; Zhu, J. Major element characteristics of sandstones and provenance analysis of basins. *Geol. China* **2007**, *34* (06), 1032−1044.
(33) Liang, B.; Wang, Q. W.; Kan, Z. Z. Geochemistry of the early jurassic muderocks feom Ziliujing formation and implications for source-area and weathering in dinosaur fossils site in Gongxian, sichuan province. *Mineral. Petrol.* **2006**, No. 03, 94−99.
(34) Rollinson, H. R. *Using Geochemical Date; Evaluation, Presentation, Interpretation*. Longman Scientific Technical, New York, 1993.
(35) Mao, G. Z.; Liu, C. Y. Application of Geochemistry in Provenance and Depositional Setting Analysis. *J. Earth Sci. Environ.* **2011**, *33* (04), 337−348.
(36) Bhatia, M. R. Rare earth elements geochemistry of Australia Paleozoic graywacks and mudrocks: Provenance and tectonic control. *Sediment. Geol.* **1985**, *45* (1/2), 97−113.
(37) Condie, K. C. Chemical composition and evolution of the upper continental crust: Contrasting results from surface samples and shales. *Chem. Geol.* **1993**, *104*, 1−37.
(38) McLennan, S. M. Relationships between the trace element composition of sedimentary rocks and upper continental crust. *Geochem. Geophy. Geosyst.* **2001**, *2* (4), No. 2000GC000109.
(39) Zhao, D. J.; Wang, X. Q. Geochemical Characteristics of the Middle Triassic Fine-grained Clastic Sedimentary Rocks in Youjiang Basin and its Implications for Provenance and Tectonic Setting. *Geotecton. Metallog.* **2020**, *44* (02), 311−324.
(40) Johnsson, M. J. The system controlling the composition of clastic sediments. *Geol. Soc. Am. Pap.* **1993**, *284*, 1−20.
(41) Yang, Z. Y.; Lang, X. H.; Tang, J. X.; Zhang, Z.; Zhang, J. S.; Gao, Y. M.; Huang, Y.; Xie, F. W.; Fu, Y. G.; Wang, Y. Geochemical Characteristics of the Jurassic Sandstones in the Xiongcun Copper-Gold Deposit, Tibet: Constraints on Tectonic Setting. *Acta Geol. Sin.* **2017**, *91* (09), 1985−2003.
(42) Nesbitt, H. W.; Young, G. M. Early Proterozoic climates and plate motions inferred from major element chemistry of lutites. *Nature* **1982**, *299*, 715−717.
(43) Fedo, C. M.; Nesbitt, H. W.; Young, G. M. Unraveling the effects of potassium metasomatism in sedimentary rocks and paleosols, with implications for paleoweathering conditions and povenance. *Geology* **1995**, *23* (10), 921−924, DOI: 10.1130/0091-7613(1995)0232.3.CO;2.
(44) Rudnick, R.; Gao, S. Composition of the continental crust. *Treatise Geochem.* **2003**, No. 3, 1−64.
(45) Xu, X. T.; Shao, L. Y. Limiting factors in utilization of chemical index of alteration of mudstones to quantify the degree of weathering in provenance. *J. Palaeogeogr.* **2018**, *20* (03), 515−522.
(46) Armstrong-Altrin, J. S.; Yong, I. L.; Verma, S. P.; Ramasamy, S. Geochemistry of sandstones from the Upper Miocene Kudankulam Formation, southern India: Implications for provenance, weathering, and tectonic setting. *J. Sediment. Res.* **2004**, *74* (2), 285−297.
(47) Nesbitt, H. W.; Young, G. M. Prediction of some weathering trends of plutonic and volcanic rocks based on thermodynamic and kinetic considerations. *Geochim. Cosmochim. Acta* **1984**, *48* (7), 1523−1534.
(48) Potter, P. E. Petrology and chemistry of modern big river sands. *J. Geol.* **1978**, *86* (4), 423−449.
(49) Roser, B. P.; Cooper, R. A.; Nathan, S.; Tulloch, A. J. Reconnaissance sandstone geochemistry, provenance, and tectonic setting of the Lower Paleozoic terranes of the West Coast and Nelson, New Zealand. *N. Z. J. Geol. Geophys.* **1996**, *39* (1), 1−16.
(50) Roser, B. P.; Korsch, R. J. Provenance signatures of sandstone-mudstone suites determined using discriminant function analysis of major-element data. *Chem. Geol.* **1988**, *67* (1−2), 119−139.
(51) Pettijohn, F. J.; Potter, P. E.; Siever, R. *Sand and Sandstone*. Springer-Verlag, New York. 1972: pp 1−553.
(52) Roser, B. P.; Korsch, R. J. Determination of tectonic setting of sandstone-mudstone suites using SiO_2 content and K_2O/Na_2O ratio. *J. Geol.* **1986**, *94* (5), 635−650.
(53) Shao, L.; Stattegger, K.; Garbe-Schoenberg, C. D. Sandstone petrology and geochemistry of the Turpan Basin (NW China): Implications for the tectonic evolution of a continental basin. *J. Sediment. Res.* **2001**, *71* (1), 37−49.
(54) Bhatia, M. R. Plate Tectonics and Geochemical composition of sandstonesv. *J. Geol.* **1983**, *91* (6), 611−627.
(55) Kumon, F.; Kiminami, K. In *Modal and Chemical Compositions of the Representative Sandstones from the Japanese Islands and Their Tectonic Implications*, Proceedings of the 29th IGC, 1994; pp 135−151.
(56) Li, Q.; Chen, Q.; Wang, J. B.; Chen, B.; Shao, H. B.; Shi, Z. H.; Gong, M. X. Elemental Geochemical Characteristics of the Sandstone Type Uranium Deposit in the Western Margin of Qaidam Basin and

https://doi.org/10.1021/acsomega.3c06163
ACS Omega 2024, 9, 3324−3341

Their Geological Significances. Bulletin of Mineralogy. *Petrol. Geochem.* **2022**, *41* (06), 1145−1164.
(57) Maynard, J. B.; Valloni, R.; Yu, H. S. Composition of modern deepsea sands from arc-related basins. *Geol. Soc.* **1982**, *10* (1), 551−561.
(58) Li, Z. Q.; Li, F. J.; Chen, Z. A.; Lai, X. L.; Ma, X. K. Provenance of Late Mesozoic Strata and Tectonic Impli-cations for the Southwestern Ordos Basin,North China:Evidence from Detrital Zircon U-Pb geochronology and Hf Isotopes. *J. Earth Sci.* **2022**, *33* (2), 373−394.
(59) Mo, N.; Guo, L.; Tong, Y.; Wang, T.; Liu, J.; Li, J. B. Geochronology, Geochemistry, Hf Isotope of Xiaojinggou Pluton in the Northern Margin of North China Craton and Its Tectonic Implications. *Acta Sci. Nat. Univ. Pek.* **2014**, *50* (06), 1021−1034.
(60) Luo, H. L.; Wu, T. R.; Zhao, L. Zicron SHRIMP U-Pb dating of Wuliangsitai A-type granite on the northern margin of the North China Plate and tectonic significance. *Acta Pet. Sin.* **2009**, *25* (3), 515−526.
(61) W, W. Q.; Liu, Z. H.; Wang, X. A.; Zhang, C.; Fan, Z. W.; Shi, Y.; Zhu, K. SHRIMP U-Pb Dating of the Zircon from the Hercynian Biotite Monzonitic Granites in Urad Zhongqi, Inner Mongolia, and Its Geological Significance. *J. Jilin Univ.* **2012**, *42* (06), 1771−1782.
(62) Zeng, J. J.; Zheng, Y. Y.; Qi, J. H.; Dai, F. H.; Zhang, G. Y.; Pang, Y. C.; Wu, B. Foundation and Geological Significance of Adakitic Granite at Guyang of Inner Mongolia. *Earth Sci.* **2008**, No. 06, 755−763.
(63) Fan, H. R.; Hu, F. F.; Yang, K. F.; Wang, K. Y.; Liu, Y. S. Geochronology framework of late Paleozoic dioritic-granitie plutons in the Bayan Obo area, Inner Mongolia, and tectonic significance. *Acta Pet. Sin.* **2009**, *25* (11), 2933−2938.
(64) Zhang, Z. B.; Xu, Y.; Miao, Y. J.; Wang, W. F.; Zhao, D. F.; Chen, D. L. Provenance and Sedimentary Environment of Paleogene Gongjue Formation in Oamdo Basin. *Acta Sedimentol. Sin.* **2022**, *40* (06), 1561−1581.
(65) Zhang, Z. B.; Zhu, Z. J.; Li, H.; Jiang, W. C.; Wang, W. F.; Xu, Y.; Li, L. R. Provenance and salt structures of gypsum formations in Pb-Zn ore-bearing Lanping Basin, Southwest China. *J. Central South Univ.* **2020**, *27* (06), 1828−1845.
(66) Chen, L. Q.; Steel, R. J.; Guo, F. S.; Olariu, C.; Gong, C. L. Alluvial fan facies of the Yongchong Basin: Implications for tectonic and paleoclimatic changes during Late Cretaceous in SE China. *J. Asian Earth Sci.* **2017**, *134*, 37−54.
(67) Wang, Y. Y.; Wu, P. Geochemical criteria of sediments in the coastal area of Jiangsu and Zhejiang Provinces. *J. Tongji Univ.* **1983**, No. 4, 82−90.
(68) Liu, G.; Zhou, D. S. Application of microelements analysis in identifying sedimentary environment: Taking Qianjiang Formation in the Jianghan basin as an example. *Pet. Geol. Exp.* **2007**, *29* (3), 307−310.
(69) Remírez, M. N.; Thomas, J. A. Paleosalinity determination in ancient epicontinental seas: A case study ofthe T-OAE in the Cleveland Basin (UK). *Earth-Sci. Rev.* **2020**, *201*, No. 103072, DOI: 10.1016/j.earscirev.2019.103072.
(70) Wei, H. Y.; Tang, Z. W.; Yan, D. T.; Wang, J. G.; Roberts, A. P. Guadalupian (Middle Permian) ocean redox evolution in South China and its implications for mass extinction. *Chem. Geol.* **2019**, *530*, 119318.
(71) Wei, H. Y.; Jiang, X. C. Early Cretaceous ferruginous and its control on the lacustrine organic matter accumulation: Constrained by multiple proxies from the Bayingebi Formation in the Bayingebi Basin, inner Mongolia, NW China. *J. Pet. Sci. Eng.* **2019**, *178*, 162−179.
(72) Qiu, Z.; Wei, H. Y.; Liu, H. L.; Shao, N.; Wang, Y. M.; Zhang, L. F.; Zhang, Q. Elementary geochemical characteristics of extraordinarily high organic matter accumulation for unconventional petroleum sedimentology. *Oil Gas Geol* **2021**, *42* (4), 91−948.
(73) Zheng, Y.; Anderson, R. F.; Geen, A.; Kuwabara, J. Authigenic molybdenum formation in marine sediments: a link to pore water sulfide in the Santa Barbara Basin. *Geochim. Cosmochim. Acta* **2000**, *64* (24), 4165−4178.
(74) Morford, J. L.; Martin, W. R.; Carney, C. M. Uranium diagenesis in sediments underlying bottom waters with high oxygen content. *Geochim. Cosmochim. Acta* **2009**, *73* (10), 2920−2937.
(75) Morford, J. L.; Martin, W. R.; Francois, R.; Carney, C. M. A model for uranium, rhenium, and molybdenum diagenesis in marine sediments based on results from coastal locations. *Geochim. Cosmochim. Acta* **2009**, *73* (10), 2938−2960.
(76) Helz, G. R.; Miller, C. V.; Charnock, J. M.; Mosselmans, J. L. W.; Pattrick, R. A. D.; Garner, C. D.; Vaughan, D. J. Mechanisms of molybdenum removal from the sea and its concentration in black shales: EXAFS evidences. *Geochim. Cosmochim. Acta* **1996**, *60* (19), 3631−3642.
(77) Tribovillard, N.; Riboulleau, A.; Lyons, T.; Baudin, F. O. Enhanced trapping of molybdenum by sulfurized organic matter of marine origin as recorded by various Mesozoic formations. *Chem. Geol.* **2004**, *213* (213), 385−401.
(78) Wei, H. Y.; Wei, X. M.; Qiu, Z.; Song, H. Y.; Shi, G. Redox conditions across the G-L boundary in South China: Evidence from pyrite morphology and sulfur isotopic compositions. *Chem. Geol.* **2016**, *440* (440), 1−14.
(79) Wei, H. Y.; Shen, J.; Schoepfer, S. D.; Krystyn, L.; Richoz, S.; Algeo, T. J. Environmental controls on marine ecosystem recovery following mass extinctions, with an example from the Early Triassic. *Earth-Sci. Rev.* **2015**, No. 149, 108−135, DOI: 10.1016/j.earscirev.2014.10.007.
(80) Wei, H. Y.; Algeo, T. J.; Yu, H.; Wang, J. G.; Guo, C.; Shi, G. Episodic euxinia in the Changhsingian (late Permian) of South China: Evidence from framboidal pyrite and geochemical data. *Sediment. Geol.* **2015**, *319*, 78−97.
(81) Calvert, S. E.; Pedersen, T. F. Geochemistry of recent oxic and anoxic marine sediments: implications for the geological record. *Mar. Geol.* **1993**, *113* (1−2), 67−88.
(82) Klinkhammer, G. P.; Palmer, M. R. Uranium in the oceans: where it goes and why. *Geochim. Cosmochim. Acta* **1991**, *55* (7), 1799−1806.
(83) Wei, H. Y.; Tang, W.; Gu, H.; Fu, X. G.; Zhang, X. Chemostratigraphy and pyrite morphology across the Wuchiapingian-Changhsingian boundary in the Middle Yangtze Platform, South China. *Geol. J.* **2021**, *56* (12), 6102−6116.
(84) Wei, H. Y.; Zhang, X.; Qiu, Z. Millennial-scale ocean redox and δ13C changes across the Permian-Triassic transition at Meishan and implications for the biocrisis. *Int. J. Earth Sci.* **2020**, *109* (5), 1753−1766.
(85) Wei, H. Y.; Tang, Z. W.; Qiu, Z.; Yan, D. T.; Bai, M. Q. Z. Formation of large carbonate concretions in black cherts in the Gufeng Formation (Guadalupian) at Enshi, South China. *Geobiology* **2020**, *18* (1), 14−30.
(86) Wei, H. Y.; Chen, D. Z.; Wang, J. G.; Yu, H.; Tucker, M. E. Organic accumulation in the lower Chihsia Formation (Middle Permian) of South China: Constraints from pyrite morphology and multiple geochemical proxies. *Palaeogeogr. Palaeoclimatol. Palaeoecol.* **2012**, *353*−*355*, 73−86.
(87) Wei, H. Y.; Chen, D. Z.; Yu, H.; Wang, J. G. End- Guadalupian mass extinction and negative carbon isotope excursion at Xiaojiaba, Guangyuan, Sichuan. *Sci. China* **2012**, *55* (9), 1480−1488.
(88) Tribovillard, N.; Algeo, T. J.; Lyons, T. W.; Riboulleau, A. Trace metals as paleoredox and paleoproductivity proxies: an update. *Chem. Geol.* **2006**, *232* (1−2), 12−32.
(89) Algeo, T. J.; Li, C. Redox classification and calibration of redox thresholds in sedimentary systems. *Geochim. Cosmochim. Acta* **2020**, *287* (287), 8−26.
(90) Algeo, T. J.; Tribovillard, N. Environmental analysis of paleoceanographic systems based on molybdenum-uranium covariation. *Chem. Geol.* **2009**, *268* (3−4), 211−225.
(91) Scott, C.; Lyons, T. W. Contrasting molybdenum cycling and isotopic properties in euxinic versus non-euxinic sediments and

https://doi.org/10.1021/acsomega.3c06163
ACS Omega 2024, 9, 3324−3341

sedimentary rocks: Refining the paleoproxies. *Chem. Geol.* **2012**, *324*−*325*, 19−27.
(92) Wang, W. Q.; Lu, C. Y.; Wang, J. Q.; Ma, H. H.; Guan, Y. Z. Characteristies of uranium content and its geological and mineral ization significance for the provenance areas, northern Northwest China. *Earth-Sci. Front.* **2019**, *26* (2), 292−303, DOI: 10.13745/j.esf.sf.2018.9.1.
(93) Ma, Y. The Occurrence and Provenance of Uranium Mineral in Hangjingi Area, Ordos Basin, Thesis; Northwest University: Xi'an, 2013.
(94) Zhao, Q. Y.; Liu, Z. H.; Wu, X. W.; Chen, X. F. Characteristics and origin of Ha Lahesshao pluton in Da Qingshan region, inner-mongolia. *Mineral. Petrol.* **2007**, *27* (1), 46−51.
(95) Xiao, X. J. The Mineralization Geochemistry of the Low Temperature Fluid on the Dongsheng Sandstone Type Uranium Deposit, Thesis; Beijing Research Institute of Uranium Geology: Beijing, 2004.
(96) Zhang, L.; Wu, B. L.; Liu, C. Y.; Lei, K. Y.; Hou, H. Q.; Sun, L.; Cun, X. N.; Wang, J. Q. Provenance Analysis of the Zhiluo Formation in the Sandstone hosted Uranium Deposits of the Northern Ordos Basin and Implications for Uranium Mineralization. *Acta Geol. Sin.* **2016**, *90* (12), 3441−3453.
(97) Yu, D. G.; Wu, R. G.; Chen, P. R.et al. *Uranium Geology*; Harbin Engineering University Press: Harbin, 2005; pp 1−450.
(98) Huang, G. N.; Huang, G. W.; Wang, W. C.; Chen, Z. L.; Yan, X.; Yu, R. A.; Zhang, C. Y. Geology and minerogenetic condition of the Lenghu sandstone-type uranium deposit in the northern margin of Qaidam Basin. *Geol. China* **2021**, *48* (4), 1200−1211.
(99) Hu, R. Z.; Bi, X. W.; Zhou, M. F.; et al. Uranium metallogenesis in South China and its relationship to crustal extension during the Cretaceous to Tertiary. *Econ. Geol.* **2008**, *103*, 583−598.
(100) Brugger, J.; Liu, W. H.; Etschmann, B.; Mei, Y.; David, M. S.; Denis, T. A review of the coordination chemistry of hydrothermal systems, or do coordination changes make ore deposits? *Chem. Geol.* **2016**, *447*, 219−253.
(101) Liu, G. Q.; Zhao, K. D.; Jiang, S. Y.; Wei, C. In-situ sulfur isotope and trace element analysis of pyrite from the Xiwang uranium ore deposit in South China: Implication for ore genesis. *J. Geochem. Explor.* **2018**, *195*, 49−65.
(102) Wu, D. H.; Pan, J. Y.; Xia, F.; Huang, G. W.; Lai, J. The mineral chemistry of chlorites and its relationship with uranium mineralization from Huangsha uranium mining area in the Middle Nanling Range,SE China. *Minerals* **2019**, *9*, 199.
(103) Jin, R. S.; Miao, P. S.; Sima, X. Z.; Li, J. G.; Zhao, H. L.; Zhao, F. Q.; Fen, X. X.; Chen, Y.; Chen, L. L.; Zhao, L. J.; Zhu, Q. Structure styles of Mesozoic-Cenozoic U-bearing rock series in Northern China. *Acta Geol. Sin.* **2016**, *90*, 2104−2116.
(104) Cheng, Y. H.; Wang, S. Y.; Jin, R. S.; Li, J. G.; Ao, C.; Teng, X. M. Global Miocene tectonics and regional sandstone-style uranium mineralization. *Ore Geol. Rev.* **2019**, *106*, 238−250.
(105) Jin, R. S.; Teng, X. M.; Li, X. G.; et al. Genesis of sandstone-type uranium deposits along the northern margin of the Ordos Basin, China. *Geosci. Front.* **2020**, *11*, 215−227.
(106) Wu, D. H. Geochemical Characteristics of Hydrothermal Alteration Minerals and Uranium Mineralization in Mianhuakeng Uranium Deposit, Northern Guangdong Province, Thesis; East China University of Technology: Nanchang, 2020.

https://doi.org/10.1021/acsomega.3c06163
ACS Omega 2024, 9, 3324−3341